PONTIFICIA UNIVERSIDAD CATÓLICA DEL PERÚ

ESCUELA DE POSGRADO

QUANTUM STATE TOMOGRAPHY FOR A POLARIZATION-PATH TWO-QUBIT OPTICAL SYSTEM

Tesis para optar el grado de Magíster en Física que presenta

DAVID REINALDO ALEJANDRO RUELAS PAREDES

Dirigido por

EDUARDO RUBÉN MASSONI KAMIMOTO

San Miguel, 2019

Quantum State Tomography for a Polarization-Path Two-Qubit Optical System

David Reinaldo Alejandro Ruelas Paredes

Propuesto para el Grado de Magíster en Física

2019

Resumen

En el área de los sistemas cuánticos abiertos, es común encontrar experimentos y modelos teóricos en los que el sistema de interés es representado por un cubit (sistema de dos niveles) y el entorno por otro cubit pese a que un entorno realista debería contener muchos más grados de libertad que el sistema con el que interactúa. No obstante, la simulación de entornos mediante un cubit es usual en la óptica cuántica, como también lo es la realización de evoluciones de sistemas de dos cubits. Los procedimientos utilizados para caracterizar los estados cuánticos producidos en el laboratorio son conocidos como tomografía de estados cuánticos. Existen algoritmos de tomografía para distintos tipos de sistemas. En esta tesis presentamos un dispositivo interferométrico que permite generar y hacer tomografía a un estado puro de un sistema de dos cubits: polarización y camino de propagación de la luz. Nuestra propuesta requiere 18 mediciones de intensidad para caracterizar cada estado. Ponemos a prueba nuestra propuesta en un experimento y contrastamos sus resultados con las predicciones teóricas.

ET LUX IN TENEBRIS LUCET
MCMXVII

Quantum State Tomography for a Polarization-Path Two-Qubit Optical System

David Reinaldo Alejandro Ruelas Paredes

Presented towards a Master's degree in Physics

2019

Abstract

In the field of open quantum systems, we usually find experiments and models in which the system is represented by a qubit (two-level system) and its environment by another qubit even though a realistic environment should contain many more degrees of freedom than the system it interacts with. However, these types of simulations are common in quantum optics, as are models of two-qubit system evolutions. The procedures that characterize quantum states produced in a laboratory are known as quantum state tomography. Standard tomography algorithms exist for different types of systems. In this thesis we present an interferometric device that allows us to generate and perform tomography on a pure polarization-path two-qubit state. 18 intensity measurements are required for characterizing each state. We test our proposal in an experiment and compare the results with the theoretical predictions.

ET LUX IN TENEBRIS LUCET
MCMXVII

Acknowledgements

There's a bunch of folks to thank, so I want to start with the only one that isn't a person. CONCYTEC-FONDECYT provided generous funding through Convenio 233-2915-2, which paid for tuition, health insurance, and a monthly wage. For all of that, I am deeply grateful.

Several people were crucial in the training I received during the past two years. Doctor candidates Elmer Suárez and Diego Barberena were the first to teach me how to work in the laboratory. Their time and efforts were invaluable; a big thank you to them. Afterwards, also-doctor-candidate Yonny Yugra helped, corrected, and guided me for some 13 months. This was already enough to be grateful to him, but then he suggested that we used polarizing beam displacers in our experiment, which turned out to be precisely what we needed. I cannot express enough gratitude for that piece of advice.

Professor Rafael Coello generously shared advice and materials. I am indebted to him, and I would like to use this chance to apologize for borrowing his instruments 3 months longer than originally agreed.

Professors Francisco De Zela and Hernán Castillo pointed out errors, missing equations, and unclear parts of an early manuscript of this thesis. I want to thank them and take responsibility for any problems remaining in the final version.

My advisor, professor Eduardo Massoni, has been crucial to the completion of this work. Were it not for his ideas, this project simply would not have existed. Thanks a lot, Eduardo.

But I was not the only one working with professor Massoni. Mariano Uria was my lab mate for the past year. His creativity and dedication are the main reasons why we managed to overcome many of the uncountably infinite difficulties of experimental physics. Thank you so much for everything.

Finally, a special mention to the two people that made my personal life easier, which was just what I needed to make up for the chaos that was work life. Dad, mom, thank you for helping me in everything so far—even now that I am an old man. Special mention to my mom, who unwittingly boosted my productivity by asking me to install Excel on my laptop. Thank you both from the bottom of my heart.

Contents

List of Figures

ET LUX IN TENEBRIS LUCET
MCMXVII

Chapter 1

Introduction

Quantum states are key objects in quantum mechanics. Given a quantum state and a set of observables, we can compute their expected values and the probabilities of measuring any of their eigenvalues. While it is customary to think of quantum states as vectors, or kets, in Hilbert spaces, there exist more general states, which are represented by density operators. All kets $|\psi\rangle$ have a corresponding density operator, $\rho = |\psi\rangle\langle\psi|$, but not all density operators can be written as kets. The states that can be written as kets are called pure states, whereas those that cannot are called mixed states.

The prescription for calculating expected values and probabilities for a quantum state is given by the postulates of quantum mechanics. This procedure is quite direct, although it scales with the number of degrees of freedom in the system. However, if we wish to test a theoretical model, we must first generate a state in the laboratory, determine from measured data what the state is, and then compute from it other quantities of interest. The procedure for reconstructing experimental states is known as quantum state tomography (QST).

The simplest systems on which to do QST are two-level quantum systems—also known as qubits—which makes them the most common in the literature. Basically any quantity that can take two excluding values can be a qubit: light polarization, which can be decomposed in two orthogonal modes, such as vertical and horizontal; light propagation path, any two paths along which a ray coming from a common source propagates; electron spin, pointing up or down a certain axis; and photon number, which can be 0 or 1 depending on whether or not a photon is detected.

Evidently, the type of QST to be performed in an experiment depends on the nature of the system under study. Polarization qubit tomography is a standard procedure. There exist algorithms for doing it on systems consisting of one [1], two [2, 3], and four polarization qubits [4]. N-qubit photonic state tomography has also been outlined [5]. The algorithm is flexible, so there exist different ways of doing it, as we shall see in Chapter 2. In ion traps, qubit tomography can be done by considering the ground and metastable states as the two levels [6]. Atomic spins in nuclear magnetic resonance [7] and quantum-dot spins [8] are other types of qubits that have also been characterised. A recently presented proposal allows for measuring either polarization or propagation path qubits in a laser light experiment [9].

Quantum mechanics is almost one hundred years old, but many of its aspects are not yet well understood. An active branch in contemporary quantum mechanics is the field of open quantum systems. Part of its importance stems, arguably, from the scientific community's burgeoning interest in information theory—which is built on the notion that information is coded in the quantum states of physical systems. Therefore, understanding how open system states evolve, and discovering optimal measurement processes is of importance for theoretical physics and a wide range of fields.

Constructing and tuning an environment in which a system's dynamics take place is, in general, a difficult and costly endeavor—more so when the environment has infinite degrees of freedom. This obstacle can be surmounted in quantum optics settings such as experiments on continuous-wave (cw), visible-range lasers or with individual photons. In these settings, we can simulate qubits in different degrees of freedom—light polarization, path of propagation, transverse mode—at a much lower cost than in, e.g., condensed matter experiments. In the literature of open quantum systems, qubits are ubiquitous. Systems of one and two qubits play the role of open systems in several theoretical models [10–14]. Moreover, qubits have also been used as environments for qubit systems—both in theory and in experiment [13, 15, 16].

Despite QST being a heavily studied set of techniques, plenty of questions remain open regarding biasedness, uncertainty, and efficiency. It is somewhat common for reconstructed quantum states to be unphysical—which means that their density matrices do not have unit trace, are not positive matrices, or are not Hermitian. For

a long time, the solution to such a problem has been to force the reconstructed matrix to be physical, which was achieved through the so-called maximum likelihood, least squares, and Bayesian estimations [2, 5, 17–19]. However, in the past few years it has been shown that all estimators that impose physicality on reconstructed density matrices are biased [20, 21]. On the other hand, uncertainties in the reconstructed quantities have always been computed by taking into account statistical fluctuations and measurement uncertainties. These procedures, which are used to compute error bars, have been called into question, and new prescriptions have been proposed [20, 22, 23]. Finally, regarding efficiency, it is well-known that even the simplest types of QST require an overcomplete set of measurements—i.e., redundant measurements. This turns into a major issue when the system size grows, for the number of measurements becomes prohibitive. Several alternatives to standard QST have been proposed with the aim of reducing the number of required measurements [24–28].

In this thesis, we will first review the basics of qubits, light polarization, the mathematical description of path and polarization degrees of freedom, polarization tomography, and two-qubit states. These concepts set up the stage for our proposal: an algorithm for characterizing pure states of a polarization-path two-qubit system. To the best of our knowledge, such an algorithm has not yet been treated in the literature, although related proposals have been tested [29]. We produced polarization-path states of laser light in a stable interferometer and used our algorithm to characterize them. After presenting our proposal, we show the results of these experiments. Finally, we summarise our work, discuss its significance, possible improvements, and point out follow-up ideas for further research.

ET LUX IN TENEBRIS LUCET
MCMXVII

Chapter 2

Preliminary Concepts

2.1 Two-level Systems

Two-level quantum systems, also called qubits, are the simplest nontrivial type of quantum systems. To do quantum mecanics on any system, we need mathematical objects called quantum states that contain information about the system. Quantum states are usually represented by vectors called kets, which live in a particular kind of vector spaces known as Hilbert spaces. The Hilbert space of a qubit is a vector space of dimension 2, so any vector in it can be written as a linear combination of two basis vectors.

Let $\{|+\rangle, |-\rangle\}$ denote an orthonormal basis in a 2-dimensional Hilbert space. Then, the most general state in said Hilbert space is given by

$$|\psi\rangle = c_1 |+\rangle + c_2 |-\rangle , \tag{2.1}$$

where c_1 and c_2, the so-called probability amplitudes, are complex numbers that satisfy $|c_1|^2 + |c_2|^2 = 1$. At first glance, it looks as if we need 4 independent real numbers to specify a qubit state. One of these parameters, however, is redundant: it accounts for a global phase, and global phases are irrelevant in quantum mechanics. With this in mind, if we write the probability amplitudes in exponential form and factor out one of the two phases, we are left with a completely equivalent state,

$$|\psi\rangle = \alpha |+\rangle + \beta e^{i\phi_\beta} |-\rangle . \tag{2.2}$$

It is evident from Eq. 2.2 that qubit states are functions of 3 real numbers: a phase, ϕ_β, and two amplitudes, α and β, such that $\alpha^2 + \beta^2 = 1$.

Alternatively, quantum states can be described by density matrices. A state described by any ket $|\psi\rangle$ is called a pure state. The same state can also be described by the density matrix $\rho = |\psi\rangle\langle\psi|$, which is an element of the set of all operators acting on the Hilbert space of $|\psi\rangle$. For example, the density matrix of $|\psi\rangle$ in Eq. 2.2 is given by

$$\rho = |\psi\rangle\langle\psi| = \alpha^2 |+\rangle\langle+| + \alpha\beta\, e^{-i\phi_\beta} |+\rangle\langle-| + \alpha\beta\, e^{i\phi_\beta} |-\rangle\langle+| + \beta^2 |-\rangle\langle-| . \tag{2.3}$$

In the basis $\{|+\rangle, |-\rangle\}$, Eq. 2.3 has the matrix representation

$$\begin{pmatrix} \alpha^2 & \alpha\beta\, e^{-i\phi_\beta} \\ \alpha\beta\, e^{i\phi_\beta} & \beta^2 \end{pmatrix}. \tag{2.4}$$

Density matrices can also describe states that kets cannot, which we call mixed states. If a system is in the state $|\psi_i\rangle$ with probability p_i, for $i = 1, \ldots, n$, then its density matrix is the weighed linear combination of proyectors, $\rho = \sum_i^n p_i |\psi_i\rangle\langle\psi_i|$. Hence, the most general qubit state can only be represented by a density matrix, not by a ket.

2.2 Path and Polarization Qubits

Experiments in quantum optics typically utilize properties of light to simulate a variety of systems. The source of this light can be either continuous wave (cw) lasers, known as classical light, or individual photons—produced in processes such as spontaneous parametric down-conversion [30, 31]—known colloquially as quantum light. As mentioned in the introduction, several kinds of qubits have been produced and characterized in different contexts. In this thesis, we will focus on two types of qubits that can be readily studied in quantum optical settings: propagation path and polarization.

2.2.1 Path Qubits

Light produced in a laser cavity can be subjected to a multitude of transformations, of which some pertain only to its path degree of freedom. Consider a beam of light travelling along a path labelled by x. We say that its state is $|x\rangle$. Suppose that this beam impinges on a mirror, making a $\pi/4$ incidence angle with respect

to an imaginary line perpendicular to the mirror. The beam will be reflected and travel along a direction perpendicular to x. Let us call this direction y. Then, the state after the beam is reflected on the mirror will be $|y\rangle$. This suggests an obvious mathematical expression for the effect of the mirror on the state of the beam. If we represent it by M, it is straightforward to note that

$$M = |x\rangle\langle y| + |y\rangle\langle x|\,, \tag{2.5}$$

where the first term accounts for the effect of the mirror on a light beam propagating along y that incides on it.

A type of instrument related to mirrors is the beam splitter (BS). Its function is simple: it divides an incident beam into a transmitted and a reflected fraction. When the two fractions are equal, the BS is said to be 50:50 (fifty-fifty). In practice, most beam splitters are not 50:50, so they must be classified according to their transmission (T) and reflection (R) coefficients. Since the sum of the transmitted and reflected fractions equals the total amount of incident light, both coefficients must satisfy $T + R = 1$. These parameters appear in the mathematical formula for beam splitters:

$$BS = \sqrt{T}(|x\rangle\langle x| + |y\rangle\langle y|) + \sqrt{R}e^{i\phi}(|x\rangle\langle y| + |y\rangle\langle x|), \tag{2.6}$$

where a phase has been included to account for the phase shift that most beam splitters add to the reflected beams. For illustrative purposes, a beam spliter is depicted in Fig. 2.1.

We have seen that mirrors and beam splitters can be expressed as linear operators. Unsurprisingly, the set of all linear operators is also a vector space. Hence, all operators that act on qubit states can be written as linear combinations of 4 basis operators. The most common basis for operators acting on path qubits is formed by the path identity operator, $\tau_0 = |x\rangle\langle x| + |y\rangle\langle y|$, and three operators equivalent to the Pauli matrices from spin-1/2 theory (albeit with different labels). The four basis operators receive the name τ matrices. In the basis of $\{|x\rangle\,, |y\rangle\}$, they are given by

$$\tau_0 = |x\rangle\langle x| + |y\rangle\langle y| = \begin{pmatrix} 1 & 0 \\ 0 & 1 \end{pmatrix}, \tag{2.7a}$$

$$\tau_1 = |x\rangle\langle x| - |y\rangle\langle y| = \begin{pmatrix} 1 & 0 \\ 0 & -1 \end{pmatrix}, \tag{2.7b}$$

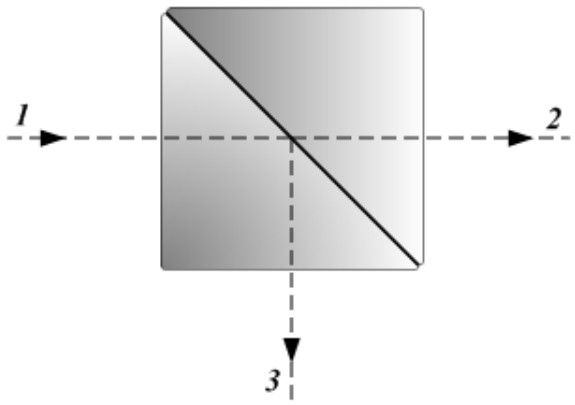

Figure 2.1: A beam splitter receives light from direction 1 and divides it into transmitted and reflected components, which travel along paths 2 and 3, respectively. Source: Wikimedia Commons.

$$\tau_2 = |x\rangle\langle y| + |y\rangle\langle x| = \begin{pmatrix} 0 & 1 \\ 1 & 0 \end{pmatrix}, \tag{2.7c}$$

$$\tau_3 = -i\,|x\rangle\langle y| + i\,|y\rangle\langle x| = \begin{pmatrix} 0 & -i \\ i & 0 \end{pmatrix}. \tag{2.7d}$$

These matrices are Hermitian, $\tau_i^\dagger = \tau_i$, and unitary, $\tau_i\tau_i^\dagger = \tau_0$. For $i = 1, 2, 3$, they are also traceless, $\operatorname{Tr}\tau_i = 0$. In the τ basis, the mirror and beam splitter operators are given by

$$M = \tau_2 \qquad \text{and} \qquad BS = \sqrt{T}\tau_0 + \sqrt{R}e^{i\phi}\tau_2. \tag{2.8}$$

The τ_i have eigenvalues $+1$ and -1. As is evident from Eqns. 2.7, the eigenvector of τ_1 corresponding to $+1$ is $|x\rangle$, and the one corresponding to -1 is $|y\rangle$. All vectors in the path space can be written in terms of these eigenvectors. In particular, the eigenvectors of τ_2 and τ_3 are

$$|2,+\rangle = \frac{1}{\sqrt{2}}(|x\rangle + |y\rangle), \qquad |2,-\rangle = \frac{1}{\sqrt{2}}(|x\rangle - |y\rangle), \tag{2.9a}$$

$$|3,+\rangle = \frac{1}{\sqrt{2}}(|x\rangle + i\,|y\rangle), \qquad |3,-\rangle = \frac{1}{\sqrt{2}}(|x\rangle - i\,|y\rangle). \tag{2.9b}$$

2.2.2 Polarization Qubits

Light can be regarded as an electromagnetic wave whose electric and magnetic fields satisfy Maxwell's equations in vacuum. Plane electromagnetic waves propagate through space following the direction of a wave vector; their component fields oscillate perpendicular to the same direction. Consider the plane perpendicular to the trajectory of a plane wave. By convention, the direction in this plane along which the electric field of the wave oscillates determines the light ray's polarization. For instance, if the electric field oscillates along the horizontal axis in the plane, the light is said to be horizontally polarized. Horizontal, vertical, diagonal (making 45° with the horizontal axis), and antidiagonal (making 135° with the horizontal axis) polarizations are types of linear polarization. Most modern commercial laser cavities produce linearly polarized states of light.

In general, light polarization is not contained in a plane[1]. The plane wave approximation is valid when the wave vector is constant or the distance travelled by light is short. For typical laboratory dimensions, laser light can be safely regarded as a plane wave.

Polarization qubits are isomorphic to path qubits—i.e., they have the same structure but with different labels. Therefore, there exists an identity operator σ_0 and three Hermitian, traceless, unitary operators, σ_i, that form a basis for operators acting on polarization qubits. We will write them in the representation where σ_1 is diagonal. Its eigenvalues $+1$ and -1 correspond to the eigenvectors $|h\rangle$ and $|v\rangle$, respectively. By analogy to Eqns. 2.7, the σ operators are

$$\sigma_0 = |h\rangle\langle h| + |v\rangle\langle v|\,, \tag{2.10a}$$

$$\sigma_1 = |h\rangle\langle h| - |v\rangle\langle v|\,, \tag{2.10b}$$

$$\sigma_2 = |h\rangle\langle v| + |h\rangle\langle v|\,, \tag{2.10c}$$

$$\sigma_3 = -i\,|h\rangle\langle v| + i\,|v\rangle\langle h|\,. \tag{2.10d}$$

As before, we can write the eigenvectors of σ_2 and σ_3 in terms of $|h\rangle$ and $|v\rangle$. They are called diagonal, antidiagonal, right-circular, and left-circular polarization, and are given by

$$|d\rangle = \frac{1}{\sqrt{2}}(|h\rangle + |v\rangle), \qquad |a\rangle = \frac{1}{\sqrt{2}}(|h\rangle - |v\rangle), \tag{2.11a}$$

[1] See Sec. 3 of [32] for a comprehensive treatment of 3-dimensional polarization states.

$$|r\rangle = \frac{1}{\sqrt{2}}(|h\rangle + i\,|v\rangle), \qquad |l\rangle = \frac{1}{\sqrt{2}}(|h\rangle - i\,|v\rangle). \tag{2.11b}$$

(Cf. 2.9.) In Sec. 2.3, we shall find a use for these eigenvectors.

One type of instruments that transform the polarization state of light are retarder wave plates. They consist of a birefringent crystal—an anisotropic medium with one refraction index along a "slow" axis and another along the orthogonal "fast" axis—which transforms the incident polarization depending on the angle its fast axis makes with, say, the vertical polarization axis.

A half-wave plate, H for short, introduces a phase shift of π between the two orthogonal components of incident light. As a consequence, it can only convert linearly polarized light into linearly polarized light. Figure 2.2 illustrates the effect of a half-wave plate on a diagonal polarization state. The phase shift can be clearly

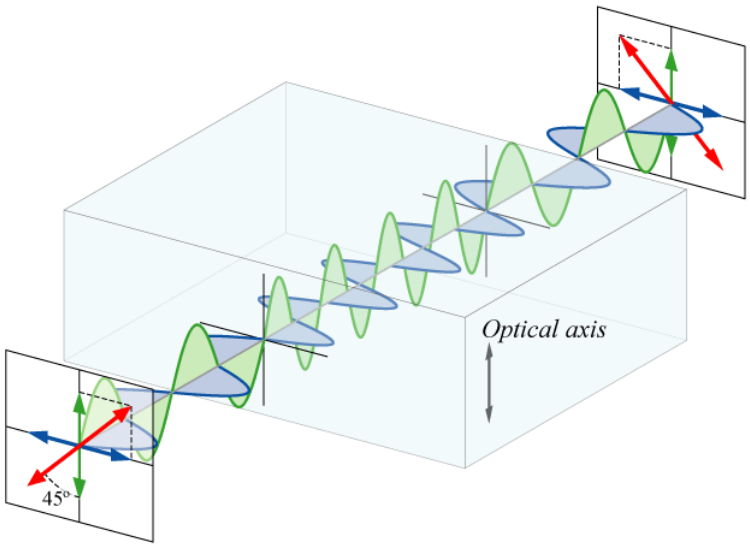

Figure 2.2: Light with diagonal polarization, depicted in red on the left, incides on a half-wave plate whose optical axis is vertical. The plate delays one of the components relative to the other and transforms the diagonal polarization into antidiagonal polarization. Source: Wikimedia Commons.

seen in the operator representation of a half-wave plate at an angle 0:

$$H(0) = |h\rangle\langle h| - |v\rangle\langle v| = e^{i0}\,|h\rangle\langle h| + e^{i\pi}\,|v\rangle\langle v|\,. \tag{2.12}$$

More in general, the operator representation of a half-wave plate at an angle θ can

be obtained by rotating Eq. 2.12 with the rotation operator,

$$R(\theta) = \cos\theta\,|h\rangle\langle h| + \sin\theta(-|h\rangle\langle v| + |v\rangle\langle h|) + \cos\theta\,|v\rangle\langle v|\,, \tag{2.13}$$

which is simply the rotation matrix in a plane, and is found to be

$$H(\theta) = R(\theta)H(0)R(-\theta) = \cos 2\theta\,|h\rangle\langle h| + \sin 2\theta(|h\rangle\langle v| + |v\rangle\langle h|) - \cos 2\theta\,|v\rangle\langle v|\,. \tag{2.14}$$

Similarly, quarter-wave plates (Q) introduce a $\pi/2$ phase difference, which allows them to transform linear polarizations into circular polarizations, and viceversa. Again, the phase difference is explicit in the expression

$$Q(0) = |h\rangle\langle h| + i\,|v\rangle\langle v| = e^{i0}\,|h\rangle\langle h| + e^{i\pi/2}\,|v\rangle\langle v|\,, \tag{2.15}$$

which is a particular case of

$$\begin{aligned} Q(\theta) = R(\theta)Q(0)R(-\theta) &= (\cos^2\theta + i\sin^2\theta)\,|h\rangle\langle h| \\ &+ (1-i)\cos\theta\sin\theta(|h\rangle\langle v| + |v\rangle\langle h|) + (\sin^2\theta + i\cos^2\theta)\,|v\rangle\langle v|\,. \end{aligned} \tag{2.16}$$

Retarder plates merely transform a polarization state and their effect is, thus, reversible. Polarizer filters, or simply polarizers, on the other hand, alter a light state in an irreversible way: they block any polarization perpendicular to the polarizer's axis, thereby erasing a component of the original state. It is evident that a polarizer, P, whose axis coincides with the horizontal direction is represented by

$$P(0) = |h\rangle\langle h|\,. \tag{2.17}$$

By performing a rotation, the general expression for a polarizer at an angle θ is found to be

$$\begin{aligned} P(\theta) &= R(\theta)P(0)R(-\theta) \\ &= \cos^2\theta\,|h\rangle\langle h| + \sin\theta\cos\theta(|h\rangle\langle v| + |v\rangle\langle h|) + \sin^2\theta\,|v\rangle\langle v|\,. \end{aligned} \tag{2.18}$$

Lastly, there are instruments that affect both the path and polarization of a beam of light. One such instrument is the polarizing beam splitter (PBS), which, as its name suggests, splits incident beams according to their polarization. Polarizing beam splitters look the same as beam splitters (Fig. 2.1), but they transmit horizontally polarized light and reflect vertically polarized light. In the path-polarization state

space, one choice of basis is the set $\{|vy\rangle, |vx\rangle, |hy\rangle, |hx\rangle\}$. In this notation, the PBS is given by

$$PBS = |hy\rangle\langle hy| + |hx\rangle\langle hx| + |vx\rangle\langle vy| + |vy\rangle\langle vx|. \tag{2.19}$$

Whereas polarizing beam splitters split light in orthogonal paths—thus greatly increasing the size of the array—polarizing beam displacers (PBDs) slightly separate a beam into two parallel paths: they transmit vertically polarized light and displace horizontally polarized light. In the right diagram of Fig. 2.3, a beam that travels

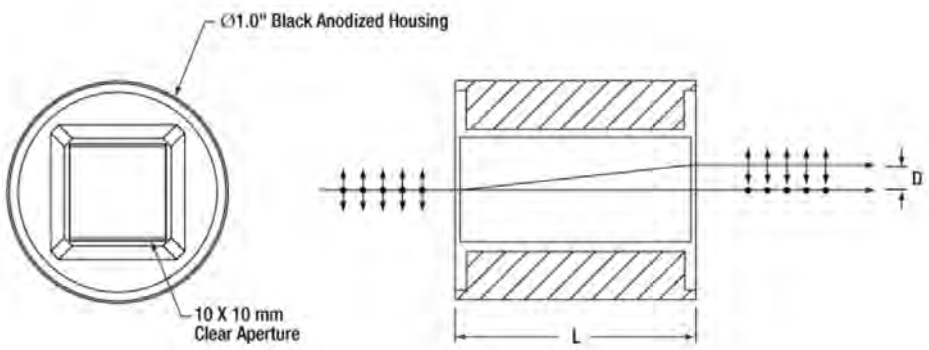

Figure 2.3: A Thorlabs mounted calcite beam displacer is shown from the front (left) and above in cross section (right). Horizontally polarized light, depicted as arrows, is displaced; vertically polarized light is directly transmitted. Source: Thorlabs.

along path y enters the PBD, which creates a displaced path, x, at a distance D from y. If the state entering the PBD is $(c_1|h\rangle + c_2|v\rangle) \otimes |y\rangle$, then the state leaving the PBD will be $c_2|vy\rangle + e^{i\phi}c_1|hx\rangle$. (The phase ϕ accounts for the phase shift introduced when one component is displaced.) The usefulness of PBDs in interferometry experiments will become evident in Chapter 3.

2.3 Polarization Tomography

Characterizing a polarization qubit is a standard procedure. While in theory it requires only 4 intensity measurements, it is commmonly done by taking 6. Section 1.4 of [1] lays out the procedure in terms of the electric field of the light beam. In this section, we will present it in the context of qubit states.

In a nutshell, polarization tomography consists of projecting the different polarization components of a beam along an axis, measuring only the projected component, and then combining the measured quantities to obtain a set of parameters that characterize the state completely. These are called Stokes parameters. To understand them, we need to further explore the mathematical structure of qubit states.

Consider a pure polarization state,

$$|p\rangle = \alpha\,|h\rangle + \beta e^{i\phi_\beta}\,|v\rangle\,, \tag{2.20}$$

with $\alpha, \beta,$ and ϕ_β real numbers. Its density operator, $\rho_p = |p\rangle\langle p|$, can be written in the σ basis. After some algebra, we find that it is given by

$$\begin{aligned}\rho_p &= \frac{\alpha^2+\beta^2}{2}\sigma_0 + \frac{\alpha^2-\beta^2}{2}\sigma_1 + \alpha\beta\cos\phi_\beta\sigma_2 + \alpha\beta\sin\phi_\beta\sigma_3 \\ &= \frac{1}{2}(\sigma_0 + \vec{\mathbf{p}}\cdot\vec{\sigma}),\ \text{with}\ \vec{\mathbf{p}} = (\alpha^2-\beta^2, 2\alpha\beta\cos\phi_\beta, 2\alpha\beta\sin\phi_\beta).\end{aligned} \tag{2.21}$$

The vector product in Eq. 2.21 is introduced for compactness, and the components of the unit vector $\vec{\mathbf{p}}$ are the Stokes parameters. As mentioned in Sec. 2.1, Eq. 2.20 is not the most general type of qubit state. Mixed states cannot be represented as kets, but they can be represented as in Eq. 2.21, with one caveat: the vector $\vec{\mathbf{p}}$ of mixed states is no longer a unit vector. Its magnitude, $|\vec{\mathbf{p}}|$, is called polarization or purity degree. If it equals 1, the state is polarized (pure); if it equals 0, the state is completely unpolarized (mixed). Intermediate values indicate partial polarization (mixture).

Measuring the Stokes parameters, p_1, p_2, p_3, of either type of state completely characterizes it. Without loss of generality, we shall illustrate how to do so for pure states. Suppose we have a beam of light whose polarization state is Eq. 2.20. First and foremost, we need to measure six intensities, i_h, i_v, i_d, i_a, i_r, i_l; these are the horizontal, vertical, diagonal, antidiagonal, circular right, and circular left polarization components of the beam. We obtain them by placing a quarter-, a half-wave plate, and a polarizer in the beam's path, conveniently setting their angles, and measuring the intensity transmitted by the polarizer. The intensities are proportional to the probabilities obtained from Eq. 2.20. One set of angles for this purpose and the intensities they correspond to are the following:

$$i_h \propto |P(\pi/2)H(\pi/4)Q(0)\,|p\rangle\,|^2 = \alpha^2, \tag{2.22a}$$

$$i_v \propto |P(\pi/2)H(0)Q(0)\,|p\rangle\,|^2 = \beta^2, \tag{2.22b}$$

$$i_d \propto |P(\pi/2)H(-\pi/8)Q(\pi/4)\,|p\rangle\,|^2 = \frac{1}{2}(\alpha^2+\beta^2+2\alpha\beta\cos\phi_\beta), \tag{2.22c}$$

$$i_a \propto |P(\pi/2)H(\pi/8)Q(\pi/4)\,|p\rangle\,|^2 = \frac{1}{2}(\alpha^2+\beta^2-2\alpha\beta\cos\phi_\beta), \tag{2.22d}$$

$$i_r \propto |P(\pi/2)H(\pi/8)Q(0)\,|p\rangle\,|^2 = \frac{1}{2}(\alpha^2+\beta^2+2\alpha\beta\sin\phi_\beta), \tag{2.22e}$$

$$i_l \propto |P(\pi/2)H(-\pi/8)Q(0)\,|p\rangle\,|^2 = \frac{1}{2}(\alpha^2+\beta^2-2\alpha\beta\sin\phi_\beta). \tag{2.22f}$$

We then subtract the intensities in 2.22 by pairs and divide them by $i_h + i_v$ to eliminate the proportionality factor. As a result, we obtain the polarization Stokes parameters:

$$p_1 = \frac{i_h - i_v}{i_h + i_v}, \qquad p_2 = \frac{i_d - i_a}{i_h + i_v}, \qquad p_3 = \frac{i_r - i_l}{i_h + i_v}. \tag{2.23}$$

Our algorithm requires a quarter-, a half-wave plate, and a polarizer. The algorithm in [1] uses only the first and the third. The extra wave plate actually simplifies our job: it allows us to measure the 6 required intensities by changing only one angle for each measurement.

2.4 Polarization-Path Systems

2.4.1 General States

One-qubit systems, as we have seen, can be described by 3 parameters. Unfortunately, two-qubit systems cannot be described by merely 6 parameters. The most general two-qubit state,

$$\rho = \frac{1}{4}\left(\sigma_0\tau_0 + \vec{\mathbf{p}}\cdot\vec{\sigma} + \vec{\mathbf{q}}\cdot\vec{\tau} + r_{ij}\sigma_i\tau_j\right), \tag{2.24}$$

has 3 polarization parameters, 3 path parameters, but depends also on 9 new quantities, the correlation parameters r_{ij}, for $i, j = 1, 2, 3$ (see, e.g., [33]). In Eq. 2.24 a sum is implied over every repeated latin index—not in $\sigma_0\tau_0$, which is simply the identity operator of the two-qubit space. To avoid clutter, we have omitted the tensor product symbol. The shorthand notation we have used stands for

$$\begin{aligned} &\sigma_0\tau_0 \equiv \sigma_0\otimes\tau_0, \qquad \vec{\sigma} \equiv (\sigma_1\otimes\tau_0, \sigma_2\otimes\tau_0, \sigma_3\otimes\tau_0), \\ &\vec{\tau} \equiv (\sigma_0\otimes\tau_1, \sigma_0\otimes\tau_2, \sigma_0\otimes\tau_3), \quad \text{and} \quad \sigma_i\tau_j \equiv \sigma_i\otimes\tau_j. \end{aligned} \tag{2.25}$$

The individual qubit states can be recovered from ρ by taking partial traces

$$\rho_{\text{pol}} = \text{Tr}_{\text{path}}\,\rho = \frac{1}{2}(\sigma_0 + \vec{\mathbf{p}}\cdot\vec{\sigma}), \qquad \rho_{\text{path}} = \text{Tr}_{\text{pol}}\,\rho = \frac{1}{2}(\tau_0 + \vec{\mathbf{q}}\cdot\vec{\tau}). \tag{2.26}$$

Analytical expressions for the 6 Stokes parameters and the 9 correlations are obtained by multiplying ρ by all the tensor products between the σ and τ matrices, and exploiting the facts that their squares equal the identity and that 6 of them are traceless. After some algebra, we find that the 15 parameters are

$$r_{ij} = \text{Tr}(\rho\,\sigma_i\tau_j), \qquad p_i = \text{Tr}(\rho\,\sigma_i\tau_0), \qquad q_j = \text{Tr}(\rho\,\sigma_0\tau_j). \tag{2.27}$$

2.4.2 Pure States

Whereas general two-qubit states depend on 15 parameters, pure two-qubit states depend only on 4 amplitudes and 3 phases:

$$|\psi\rangle = \alpha\,|vy\rangle + \beta\,e^{i\phi_\beta}\,|vx\rangle + \gamma\,e^{i\phi_\gamma}\,|hy\rangle + \delta\,e^{i\phi_\delta}\,|hx\rangle\,; \tag{2.28}$$

the amplitudes satisfy $\alpha^2+\beta^2+\gamma^2+\delta^2 = 1$, so technically the state depends only on 6 quantities. In the $\{|vy\rangle, |vx\rangle, |hy\rangle, |hx\rangle\}$ basis, the density matrix of $|\psi\rangle$ has the form

$$\begin{pmatrix} \alpha^2 & \alpha\beta\,e^{-i\phi_\beta} & \alpha\gamma\,e^{-i\phi_\gamma} & \alpha\delta\,e^{-i\phi_\delta} \\ \alpha\beta\,e^{i\phi_\beta} & \beta^2 & \beta\gamma\,e^{i(\phi_\beta-\phi_\gamma)} & \beta\delta\,e^{i(\phi_\beta-\phi_\delta)} \\ \alpha\gamma\,e^{i\phi_\gamma} & \beta\gamma\,e^{-i(\phi_\beta-\phi_\gamma)} & \gamma^2 & \gamma\delta\,e^{i(\phi_\gamma-\phi_\delta)} \\ \alpha\delta\,e^{i\phi_\delta} & \beta\delta\,e^{-i(\phi_\beta-\phi_\delta)} & \gamma\delta\,e^{-i(\phi_\gamma-\phi_\delta)} & \delta^2 \end{pmatrix}. \tag{2.29}$$

By directly applying Eqns. 2.27, the Stokes and correlation parameters of the pure state are found to be

$$p_1 = -\alpha^2 - \beta^2 + \gamma^2 + \delta^2, \tag{2.30a}$$

$$p_2 = 2\alpha\gamma\cos\phi_\gamma + 2\beta\delta\cos(\phi_\beta - \phi_\delta), \tag{2.30b}$$

$$p_3 = -2\alpha\gamma\sin\phi_\gamma + 2\beta\delta\sin(\phi_\beta - \phi_\delta), \tag{2.30c}$$

$$q_1 = -\alpha^2 + \beta^2 - \gamma^2 + \delta^2, \tag{2.31a}$$

$$q_2 = 2\alpha\beta\cos\phi_\beta + 2\gamma\delta\cos(\phi_\gamma - \phi_\delta), \tag{2.31b}$$

$$q_3 = -2\alpha\beta\sin\phi_\beta + 2\gamma\delta\sin(\phi_\gamma - \phi_\delta), \tag{2.31c}$$

$$r_{11} = \alpha^2 - \beta^2 - \gamma^2 + \delta^2, \tag{2.32a}$$

$$r_{12} = -2\alpha\beta\cos\phi_\beta + 2\gamma\delta\cos(\phi_\gamma - \phi_\delta), \tag{2.32b}$$

$$r_{13} = 2\alpha\beta\sin\phi_\beta + 2\gamma\delta\sin(\phi_\gamma - \phi_\delta), \tag{2.32c}$$

$$r_{21} = -2\alpha\gamma\cos\phi_\gamma + 2\beta\delta\cos(\phi_\beta - \phi_\delta), \tag{2.32d}$$

$$r_{22} = 2\beta\gamma\cos(\phi_\beta - \phi_\gamma) + 2\alpha\delta\cos\phi_\delta, \tag{2.32e}$$

$$r_{23} = -2\beta\gamma\sin(\phi_\beta - \phi_\gamma) - 2\alpha\delta\sin\phi_\delta, \tag{2.32f}$$

$$r_{31} = 2\alpha\gamma\sin\phi_\gamma + 2\beta\delta\sin(\phi_\beta - \phi_\delta), \tag{2.32g}$$

$$r_{32} = 2\beta\gamma\sin(\phi_\beta - \phi_\gamma) - 2\alpha\delta\sin\phi_\delta, \tag{2.32h}$$

$$r_{33} = 2\beta\gamma\cos(\phi_\beta - \phi_\gamma) - 2\alpha\delta\cos\phi_\delta. \tag{2.32i}$$

Evidently, since these 15 parameters are functions of 7 quantities, not all of the above expressions are linearly independent. Although somewhat redundant, describing a pure state by Eqns. 2.30, 2.31, and 2.32 is completely equivalent to specifying the 7 parameters in Eq. 2.28.

Chapter 3

Experimental Proposal and Realization

We wish to do quantum state tomography on a state of the form of Eq. 2.28. To this end, we present a device that allows us to measure a set of intensities from which all the pure state parameters can be computed. This procedure can, in theory, be carried out in a Mach-Zehnder interferometer, where it is conceptually easy to understand (Sec. 3.1). Practical considerations, however, make it extremely difficult to complete the measurements in this set up. Therefore, we devised an equivalent device: an interferometer with two polarizing beam displacers (PBDs) and no mirrors (Sec. 3.2). This interferometer was used to generate and characterize the set of states described in Sec. 3.3.

3.1 Mach-Zehnder Device

Consider the Mach-Zehnder interferometer in Fig. 3.1. It consists of two parts: one generates arbitrary two-qubit pure states; the other characterizes them. In the generation stage, a horizontally polarized beam of light passes through a half-wave plate at an angle θ, after which it is divided by a polarizing beam splitter (PBS). The transmitted component is subjected to some transformation, T_1; the reflected component, to T_2. Because the states of light in each arm are linearly polarized, it is possible, by choosing T_1 and T_2 to be a half-wave plate followed by a quarter-

wave plate, to transform both into arbitrary polarization states[1]. By adjusting the lengths of both arms, a relative phase difference between them can be added. The combination of this phase shift, T_1, and T_2 creates an arbitrary two-qubit pure state. After leaving the generation part of the array, the two rays are reflected by mirrors, M, and enter the characterization device.

To carry out two-qubit pure state tomography, the array described so far must be completed with the instruments contained in the dashed rectangle on the top right of Fig. 3.1. The diagram shows a half-wave plate, $H(\phi)$, placed in the transmitted arm; its angle will take two values: 0 and $\pi/4$. Following the plate is a PBS that combines the beams in the reflected and transmitted arms. Finally, at both PBS exits, the polarization tomography of Sec. 2.3 is done by placing a quarter-, a half-wave plate, a polarizer, and a powermeter. Repeating this procedure in both arms for both values of ϕ yields a set of intensities that can characterize the state completely. When $\phi = 0$ ($\phi = \pi/4$) the intensities will be labelled by an unprimed (primed) subscript. The intensities measured in the horizontal (vertical) arm will be denoted i_x and $i_{x'}$ (i_y and $i_{y'}$).

Let us look with more detail at these intensities. After the generation stage, the beams in both arms are reflected in the mirrors, so the state becomes

$$(\alpha\,|v\rangle + \gamma\, e^{i\phi_\gamma}\,|h\rangle) \otimes |x\rangle + (\beta\, e^{i\phi_\beta}\,|v\rangle + \delta\, e^{i\phi_\delta}\,|h\rangle) \otimes |y\rangle\,. \tag{3.1}$$

The half-wave plate $H(\phi)$ determines two cases. For $\phi = 0$, the state coming out of the PBS is

$$(-\beta\, e^{i\phi_\beta}\,|v\rangle + \gamma\, e^{i\phi_\gamma}\,|h\rangle) \otimes |x\rangle + (\alpha\,|v\rangle + \delta\, e^{i\phi_\delta}\,|h\rangle) \otimes |y\rangle\,. \tag{3.2}$$

We then do polarization tomography in both arms. By adopting the naming convention of Sec. 2.3, the intensities thus obtained will be $i_{xh}, \ldots, i_{xl}$ and $i_{yh}, \ldots, i_{yl}$. For normalization purposes, we define $i_t \equiv i_{xh} + i_{xv} + i_{yh} + i_{yv}$. It can be readily seen that the normalized, unprimed intensities are

$$\frac{i_{xh}}{i_t} = \gamma^2, \tag{3.3a}$$

$$\frac{i_{xv}}{i_t} = \beta^2, \tag{3.3b}$$

[1]See Sec. 4.6.4 of [1] for a geometrical explanation of this HQ gadget.

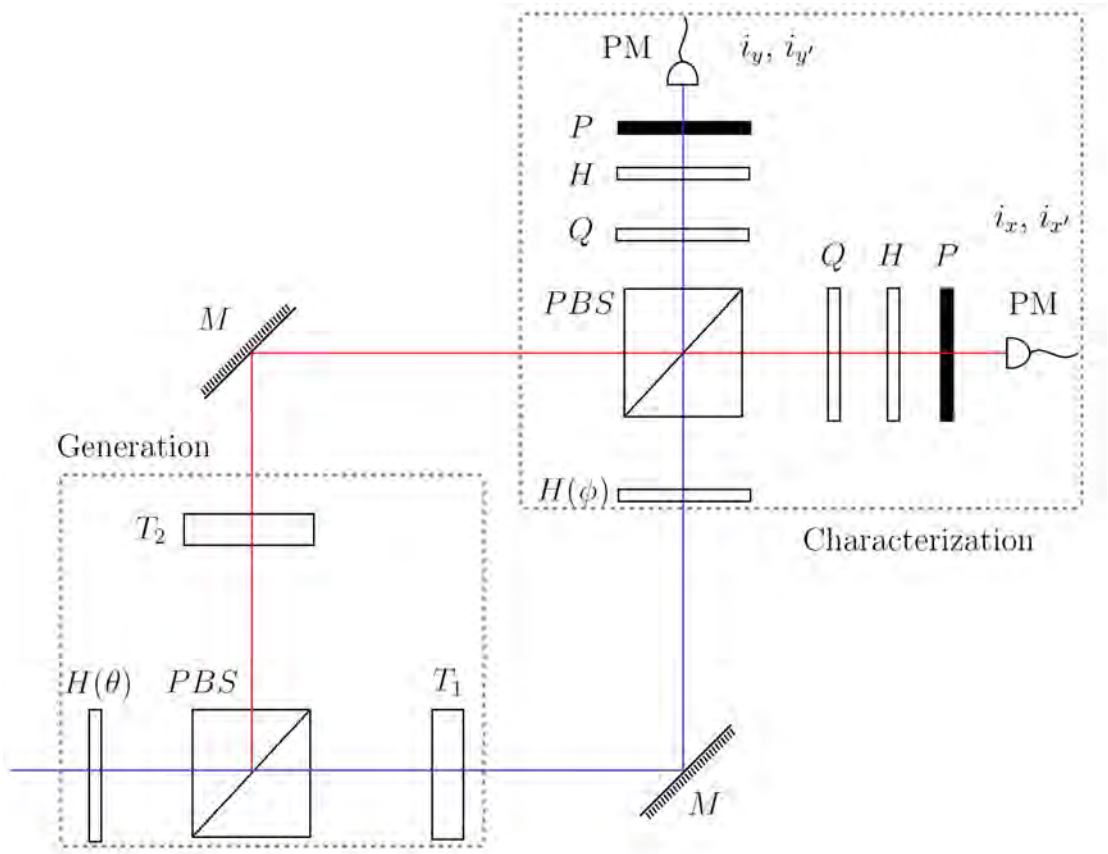

Figure 3.1: A Mach-Zehnder interferometer that consists of two parts: one for state generation; the other, for characterization. A half-wave plate, $H(\theta)$, a polarizing beam splitter (PBS), and two transformations, T_1 and T_2, produce a general polarization-path pure state. To completely characterize said state, an additional half-wave plate, $H(\phi)$, is put in one of the interferometer arms. Its angle determines two sets of intensities: those with unprimed subscripts, for $\phi = 0$, and those with primed subscripts, for $\phi = \pi/4$. At the exits of a second PBS, polarization tomography is carried out by using a QHP gadget followed by a powermeter (PM). The intensities measured in the horizontal arm will be labelled i_x and $i_{x'}$; the ones in the vertical arm will be i_y and $i_{y'}$.

$$\frac{i_{xd}}{i_t} = \frac{1}{2}[\beta^2 + \gamma^2 - 2\beta\gamma\cos(\phi_\beta - \phi_\gamma)], \tag{3.3c}$$

$$\frac{i_{xa}}{i_t} = \frac{1}{2}[\beta^2 + \gamma^2 + 2\beta\gamma\cos(\phi_\beta - \phi_\gamma)], \tag{3.3d}$$

$$\frac{i_{xr}}{i_t} = \frac{1}{2}[\beta^2 + \gamma^2 - 2\beta\gamma\sin(\phi_\beta - \phi_\gamma)], \tag{3.3e}$$

$$\frac{i_{xl}}{i_t} = \frac{1}{2}[\beta^2 + \gamma^2 + 2\beta\gamma\sin(\phi_\beta - \phi_\gamma)], \tag{3.3f}$$

$$\frac{i_{yh}}{i_t} = \delta^2, \tag{3.4a}$$
$$\frac{i_{yv}}{i_t} = \alpha^2, \tag{3.4b}$$
$$\frac{i_{yd}}{i_t} = \frac{1}{2}(\alpha^2 + \delta^2 + 2\alpha\delta\cos\phi_\delta), \tag{3.4c}$$
$$\frac{i_{ya}}{i_t} = \frac{1}{2}(\alpha^2 + \delta^2 - 2\alpha\delta\cos\phi_\delta), \tag{3.4d}$$
$$\frac{i_{yr}}{i_t} = \frac{1}{2}(\alpha^2 + \delta^2 - 2\alpha\delta\sin\phi_\delta), \tag{3.4e}$$
$$\frac{i_{yl}}{i_t} = \frac{1}{2}(\alpha^2 + \delta^2 + 2\alpha\delta\sin\phi_\delta). \tag{3.4f}$$

On the other hand, for $\phi = \pi/4$, the state coming out of the PBS is

$$(\delta\, e^{i\phi_\delta}\,|v\rangle + \gamma\, e^{i\phi_\gamma}\,|h\rangle) \otimes |x\rangle + (\alpha\,|v\rangle + \beta\, e^{i\phi_\beta}\,|h\rangle) \otimes |y\rangle\,, \tag{3.5}$$

and the tomography intensities are

$$\frac{i_{x'h}}{i_t} = \gamma^2, \tag{3.6a}$$
$$\frac{i_{x'v}}{i_t} = \delta^2, \tag{3.6b}$$
$$\frac{i_{x'd}}{i_t} = \frac{1}{2}[\gamma^2 + \delta^2 + 2\gamma\delta\cos(\phi_\gamma - \phi_\delta)], \tag{3.6c}$$
$$\frac{i_{x'a}}{i_t} = \frac{1}{2}[\gamma^2 + \delta^2 - 2\gamma\delta\cos(\phi_\gamma - \phi_\delta)], \tag{3.6d}$$
$$\frac{i_{x'r}}{i_t} = \frac{1}{2}[\gamma^2 + \delta^2 - 2\gamma\delta\sin(\phi_\gamma - \phi_\delta)], \tag{3.6e}$$
$$\frac{i_{x'l}}{i_t} = \frac{1}{2}[\gamma^2 + \delta^2 + 2\gamma\delta\sin(\phi_\gamma - \phi_\delta)], \tag{3.6f}$$

$$\frac{i_{y'h}}{i_t} = \beta^2, \tag{3.7a}$$
$$\frac{i_{y'v}}{i_t} = \alpha^2, \tag{3.7b}$$
$$\frac{i_{y'd}}{i_t} = \frac{1}{2}(\alpha^2 + \beta^2 + 2\alpha\beta\cos\phi_\beta), \tag{3.7c}$$
$$\frac{i_{y'a}}{i_t} = \frac{1}{2}(\alpha^2 + \beta^2 - 2\alpha\beta\cos\phi_\beta), \tag{3.7d}$$
$$\frac{i_{y'r}}{i_t} = \frac{1}{2}(\alpha^2 + \beta^2 - 2\alpha\beta\sin\phi_\beta), \tag{3.7e}$$
$$\frac{i_{y'l}}{i_t} = \frac{1}{2}(\alpha^2 + \beta^2 + 2\alpha\beta\sin\phi_\beta). \tag{3.7f}$$

Evidently, i_t is also equal to $i_{x'h} + i_{x'v} + i_{y'h} + i_{y'v}$.

We started off with the goal of obtaining the parameters of Eq. 2.28. Much to our joy, only 18 intensities, $i_{x'}$, $i_{y'}$, and i_y, are required for our purposes. Explicitly, the parameters are related to the intensities by

$$\alpha^2 = \frac{i_{yv}}{i_t} = \frac{i_{y'v}}{i_t}, \quad \beta^2 = \frac{i_{y'h}}{i_t}, \quad \gamma^2 = \frac{i_{x'h}}{i_t}, \quad \delta^2 = \frac{i_{yh}}{i_t} = \frac{i_{x'v}}{i_t}, \tag{3.8}$$

and

$$\phi_\beta = \arctan\left(\frac{i_{y'l} - i_{y'r}}{i_{y'd} - i_{y'a}}\right), \tag{3.9a}$$

$$\phi_\delta = \arctan\left(\frac{i_{yl} - i_{yr}}{i_{yd} - i_{ya}}\right), \tag{3.9b}$$

$$\phi_\gamma = \arctan\left(\frac{i_{x'l} - i_{x'r}}{i_{x'd} - i_{x'a}}\right) + \phi_\delta. \tag{3.9c}$$

If, instead, we wished to compute the Stokes and correlation parameters, we would need the sines and cosines in Eqns. 2.30, 2.31, and 2.32. Some can be found directly; namely,

$$\cos\phi_\delta = \frac{i_{yd} - i_{ya}}{2\alpha\delta\, i_t}, \tag{3.10}$$

$$\sin\phi_\delta = \frac{i_{yl} - i_{yr}}{2\alpha\delta\, i_t}, \tag{3.11}$$

$$\cos(\phi_\gamma - \phi_\delta) = \frac{i_{x'd} - i_{x'a}}{2\gamma\delta\, i_t}, \tag{3.12}$$

$$\sin(\phi_\gamma - \phi_\delta) = \frac{i_{x'l} - i_{x'r}}{2\gamma\delta\, i_t}, \tag{3.13}$$

$$\cos\phi_\beta = \frac{i_{y'd} - i_{y'a}}{2\alpha\beta\, i_t}, \tag{3.14}$$

$$\sin\phi_\beta = \frac{i_{y'l} - i_{y'r}}{2\alpha\beta\, i_t}. \tag{3.15}$$

Afterwards, quantities such as $\cos\phi_\gamma$ can be computed by using angle sum identities.

While our algorithm is quite straightforward, it is not free of a common practical complication: the notorious instability of Mach-Zehnder interferometers. Instabilities stem from perturbations such as mechanical vibrations, wind currents, and temperature fluctuations, which alter the relative positions of mirrors and beam splitters. Their combined effects can render any measurements insignificant. Logically, the effect of perturbations could be significantly reduced by employing less mirrors or PBSs. Such an alternative set up is feasible, and will be the subject of the next section.

3.2 Beam Displacer Device

An interferometer which uses PBDs instead of PBSs requires no mirrors and its arms are shorter than those of Mach-Zehnder and Sagnac interferometers. It should, at least in theory, be much more stable than them. We used such an interferometer for our experiments. The results (Chapter 4) point to an unequivocal conclusion: the PBD interferometer is incomparably much more stable than the alternatives.

Figure 3.2 illustrates our interferometer and its two modes of use. In the beginning, it works exactly like the Mach-Zehnder interferometer: a horizontally-polarized light ray passes through a half-wave plate, $H(\theta)$, enters a PBD and is divided into two paths. Vertical polarization is transmitted along path y, while horizontal polarization is displaced along path x. The same transformations of Fig. 3.1 are performed on the respective paths—T_1 on path x, T_2 on path y—albeit in a much more reduced space. At this point, the two-qubit pure state has been generated.

For the tomography stage, we first place a half-wave plate $H(\phi)$ following T_1. Next up, we could place a second PBD and observe a new path emerge. It would contain the horizontally-polarized beam displaced from path x. Which of the three paths exiting the PBD, if any, gives us the intensities of Eqns. 3.3, 3.4, 3.6, and 3.7? The answer is not immediately obvious because PBDs function differently from PBSs. To obtain the desired outcomes, we must place two additional half-wave plates in our array—one before the second PBD and another after it. The angles on these plates will be either 0 or $\pi/4$ depending on whether we wish to measure i_x, $i_{x'}$ or i_y, $i_{y'}$. For $\phi = 0$, the state entering the H-PBD-H gadget is

$$(\alpha\,|v\rangle + \gamma\, e^{i\phi_\gamma}\,|h\rangle) \otimes |y\rangle + (-\beta\, e^{i\phi_\beta}\,|v\rangle + \delta\, e^{i\phi_\delta}\,|h\rangle) \otimes |x\rangle\,. \tag{3.16}$$

This state then passes through $H(0)$ and the PBD. Upon exiting, only its x-component passes through another $H(0)$. Mathematically,

$$\begin{aligned}
&\xrightarrow{H(0)} (-\alpha\,|v\rangle + \gamma\, e^{i\phi_\gamma}\,|h\rangle) \otimes |y\rangle + (\beta\, e^{i\phi_\beta}\,|v\rangle + \delta\, e^{i\phi_\delta}\,|h\rangle) \otimes |x\rangle \\
&\xrightarrow{|x\rangle\langle x|PBD} (\beta\, e^{i\phi_\beta}\,|v\rangle + \gamma\, e^{i\phi_\gamma}\,|h\rangle) \otimes |x\rangle \\
&\xrightarrow{H(0)} (-\beta\, e^{i\phi_\beta}\,|v\rangle + \gamma\, e^{i\phi_\gamma}\,|h\rangle) \otimes |x\rangle
\end{aligned} \tag{3.17}$$

(cf. the first term in Eq. 3.2). When both plates are at $\pi/4$ we obtain

$$\xrightarrow{H(\pi/4)} (\alpha\,|h\rangle + \gamma\, e^{i\phi_\gamma}\,|v\rangle) \otimes |y\rangle + (-\beta\, e^{i\phi_\beta}\,|h\rangle + \delta\, e^{i\phi_\delta}\,|v\rangle) \otimes |x\rangle$$

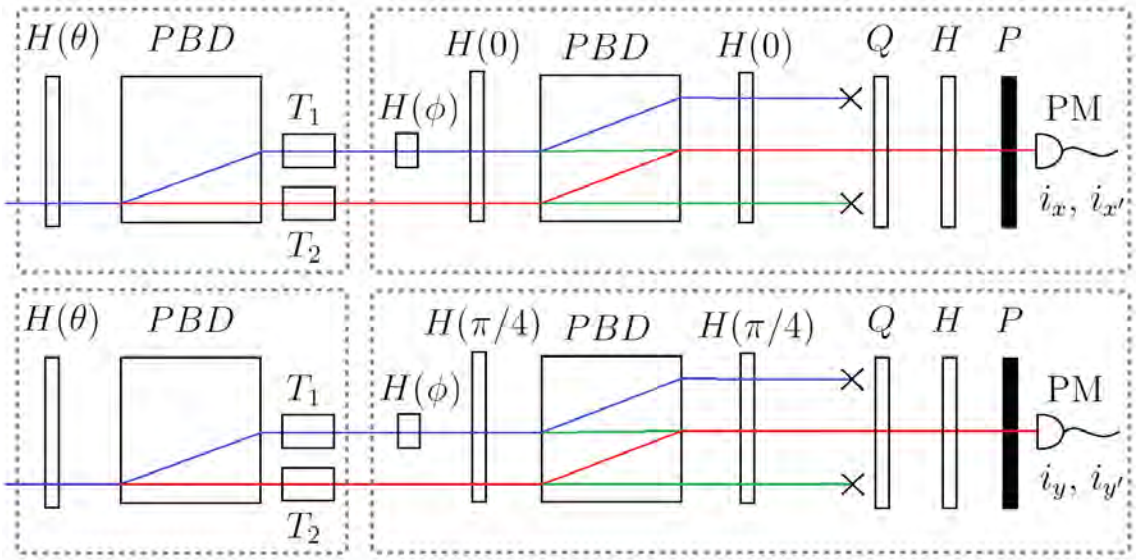

Figure 3.2: The two configurations of our interferometric device. In both diagrams, the dashed boxes on the left enclose the state generation stage. A light beam with horizontal polarization enters the array after passing through $H(\theta)$. The resulting state has a vertical component, transmitted along path y by a polarizing beam displacer (PBD), and a horizontal component, displaced by the PBD (thereby gaining a phase) along path x. Each individual beam is then subjected to some transformation, T_1 or T_2. The dashed boxes on the right contain the tomography stage. A half-wave plate in the x path, $H(\phi)$, determines two types of intensities: those with primed subscripts, when $\phi = \pi/4$, and those with unprimed subscripts, for $\phi = 0$. To measure all the required intensities, two additional half-wave plates are needed—one before and one after the second PBD. To obtain the i_x and $i_{x'}$ (i_y and $i_{y'}$) intensities of Fig. 3.1, both these plates must be at an angle of 0 ($\pi/4$). At the second PBD, the beams transmitted from arm y and reflected from arm x are blocked out. Finally, polarization tomography is carried out on the beam exiting the interferometer by using a QHP gadget followed by a powermeter (PM).

$$\begin{aligned} &\xrightarrow{|x\rangle\langle x|PBD}(\alpha\,|h\rangle + \delta\, e^{i\phi_\delta}\,|v\rangle)\otimes|x\rangle \\ &\xrightarrow{H(\pi/4)}(\alpha\,|v\rangle + \delta\, e^{i\phi_\delta}\,|h\rangle)\otimes|x\rangle \end{aligned} \tag{3.18}$$

(cf. the second term in Eq. 3.2). Similarly, for $\phi = \pi/4$ the state before the H-PBD-H gadget is

$$(\alpha\,|v\rangle + \gamma\, e^{i\phi_\gamma}\,|h\rangle)\otimes|y\rangle + (\beta\, e^{i\phi_\beta}\,|h\rangle + \delta\, e^{i\phi_\delta}\,|v\rangle)\otimes|x\rangle\,. \tag{3.19}$$

Again, the transformations

$$\begin{aligned}
&\xrightarrow{H(0)}(-\alpha\,|v\rangle+\gamma\,e^{i\phi_\gamma}\,|h\rangle)\otimes|y\rangle+(\beta\,e^{i\phi_\beta}\,|h\rangle-\delta\,e^{i\phi_\delta}\,|v\rangle)\otimes|x\rangle\\
&\xrightarrow{|x\rangle\langle x|PBD}(\gamma\,e^{i\phi_\gamma}\,|h\rangle-\delta\,e^{i\phi_\delta}\,|v\rangle)\otimes|x\rangle\\
&\xrightarrow{H(0)}(\gamma\,e^{i\phi_\gamma}\,|h\rangle+\delta\,e^{i\phi_\delta}\,|v\rangle)\otimes|x\rangle
\end{aligned}\tag{3.20}$$

yield the intensities $i_{x'}$ (cf. the first term in Eq. 3.5), whereas

$$\begin{aligned}
&\xrightarrow{H(\pi/4)}(\alpha\,|h\rangle+\gamma\,e^{i\phi_\gamma}\,|v\rangle)\otimes|y\rangle+(\beta\,e^{i\phi_\beta}\,|v\rangle+\delta\,e^{i\phi_\delta}\,|h\rangle)\otimes|x\rangle\\
&\xrightarrow{|x\rangle\langle x|PBD}(\alpha\,|h\rangle+\beta\,e^{i\phi_\beta}\,|v\rangle)\otimes|x\rangle\\
&\xrightarrow{H(\pi/4)}(\alpha\,|v\rangle+\beta\,e^{i\phi_\beta}\,|h\rangle)\otimes|x\rangle
\end{aligned}\tag{3.21}$$

give us the $i_{y'}$ (cf. the second term in Eq. 3.5).

3.3 Experimental Realization

In our experiments, we used the interferometer depicted in Fig. 3.2. For simplicity, we took T_1 to be the identity, and $T_2 = H(\phi_2)$. Since it is virtually impossible for the lengths of the interferometer's arms to be identical, there is a phase difference between both. In our calculations, we call this phase ϕ_1 and insert it in arm y. Determining ϕ_1 will be of importance for our results. With this in mind, the state produced in our array is

$$\begin{aligned}
|\psi\rangle &= \left(|x\rangle\langle x| + e^{i\phi_1}\,H(\phi_2)\,|y\rangle\langle y|\right)(PBD)\,H(\theta)\,|hy\rangle\\
&= \cos 2\phi_2 \sin 2\theta\,|vy\rangle + \sin 2\phi_2 \sin 2\theta\,e^{i\pi}\,|hy\rangle + \cos 2\theta\,e^{i(\pi-\phi_1)}\,|hx\rangle\\
&= \cos 2\phi_2 \sin 2\theta\,|vy\rangle - \sin 2\phi_2 \sin 2\theta\,|hy\rangle - \cos 2\theta\,e^{-i\phi_1}\,|hx\rangle\,.
\end{aligned}\tag{3.22}$$

By comparing Eq. 3.22 to Eq. 2.28, the state parameters are found to be

$$\begin{gathered}
\alpha = \cos 2\phi_2 \sin 2\theta, \quad \beta = 0, \quad \gamma = \sin 2\phi_2 \sin 2\theta, \quad \delta = \cos 2\theta,\\
\phi_\beta = 0, \quad \phi_\gamma = \pi, \quad \phi_\delta = \pi - \phi_1.
\end{gathered}\tag{3.23}$$

For reference, the Stokes and correlation parameters of the state in Eq. 3.22 are

$$p_1 = \frac{1}{4}\left[2 + 2\cos 4\theta + \cos(4\theta - 4\phi_2) - 2\cos 4\phi_2 + \cos(4\theta + 4\phi_2)\right], \tag{3.24a}$$

$$p_2 = -\sin^2 2\theta \sin 4\phi_2, \tag{3.24b}$$

$$p_3 = 0, \tag{3.24c}$$

$$q_1 = \cos 4\theta, \tag{3.25a}$$

$$q_2 = \sin 4\theta \sin 2\phi_2 \cos \phi_1, \tag{3.25b}$$

$$q_3 = \sin 4\theta \sin 2\phi_2 \sin \phi_1, \tag{3.25c}$$

$$r_{11} = \frac{1}{4}\left[2 + 2\cos 4\theta - \cos(4\theta - 4\phi_2) + 2\cos 4\phi_2 - \cos(4\theta + 4\phi_2)\right], \tag{3.26a}$$

$$r_{12} = \sin 4\theta \sin 2\phi_2 \cos \phi_1, \tag{3.26b}$$

$$r_{13} = \sin 4\theta \sin 2\phi_2 \sin \phi_1, \tag{3.26c}$$

$$r_{21} = \sin^2 2\theta \sin 4\phi_2, \tag{3.26d}$$

$$r_{22} = -\sin 4\theta \cos 2\phi_2 \cos \phi_1, \tag{3.26e}$$

$$r_{23} = -\sin 4\theta \cos 2\phi_2 \sin \phi_1, \tag{3.26f}$$

$$r_{31} = 0, \tag{3.26g}$$

$$r_{32} = -\sin 4\theta \cos 2\phi_2 \sin \phi_1, \tag{3.26h}$$

$$r_{33} = \sin 4\theta \cos 2\phi_2 \cos \phi_1. \tag{3.26i}$$

In the actual array, the angle θ of the first half-wave plate took the values 0°, 10°, 20°, ..., 80°. The angle of the half-wave plate in arm y was fixed at $\phi_2 = \pi/8$. A Helium-Neon cw laser of wavelength 633 nm was used as a source of linearly polarized light.

ET LUX IN TENEBRIS LUCET
MCMXVII

Chapter 4

Results

We performed the 18 intensity measurements described in Sec. 3.2 for 9 different polarization-path states. These intensities were then used to compute the Stokes and correlations parameters of the 9 states. In this chapter, we present the results and compare them to the theoretical predictions.

4.1 Polarization Stokes Parameters

Polarization tomography can be carried out either inside the interferometer—by doing standard polarization tomography on the two beams simultaneously, thereby tracing over the path—or outside it, after the second PBD, as described in Sec. 3.2. Since the first method is not affected by interference in the second beam displacer, it should be more stable than the second. Additionally, it requires only 6 intensity measurements, whereas the second requires 18. We used both methods and obtained nearly identical results.

According to Eqn. 3.23, the polarization Stokes parameters should be given by

$$p_1 = \frac{1}{2}\left(1 + \cos 4\theta\right), \tag{4.1a}$$

$$p_2 = -\sin^2 2\theta, \tag{4.1b}$$

$$p_3 = 0. \tag{4.1c}$$

The results we obtained are shown in Figs. 4.1–4.3. The blue curves are given by Eqns. 4.1; the red dots represent the experimental polarization Stokes parameters p_1, p_2, and p_3.

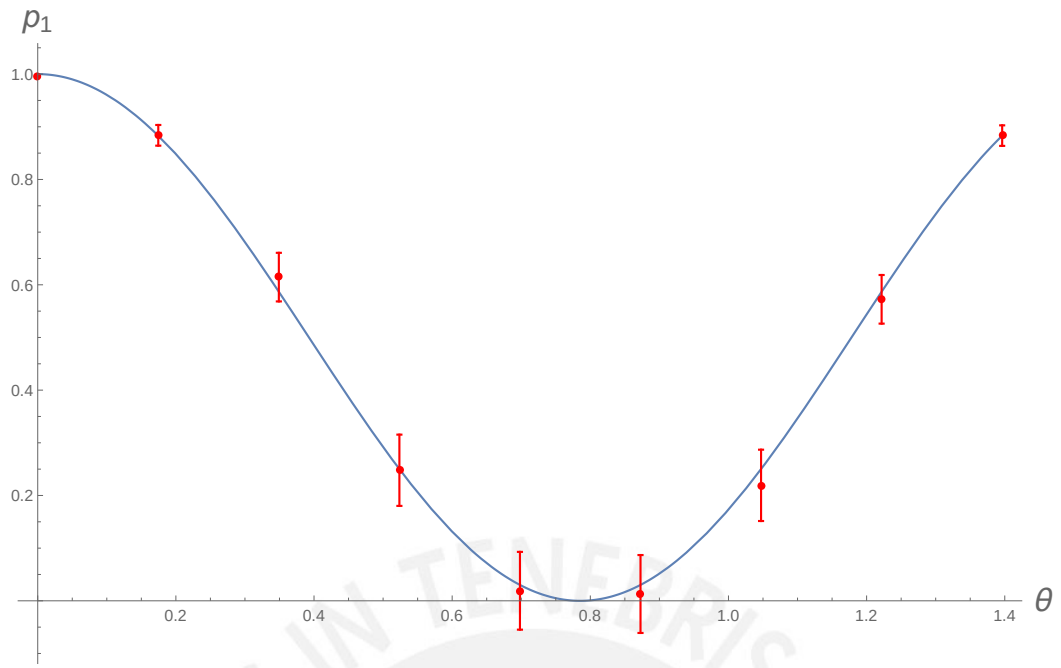

Figure 4.1: Theoretical (blue curve) and experimental (red dots) polarization Stokes parameter p_1.

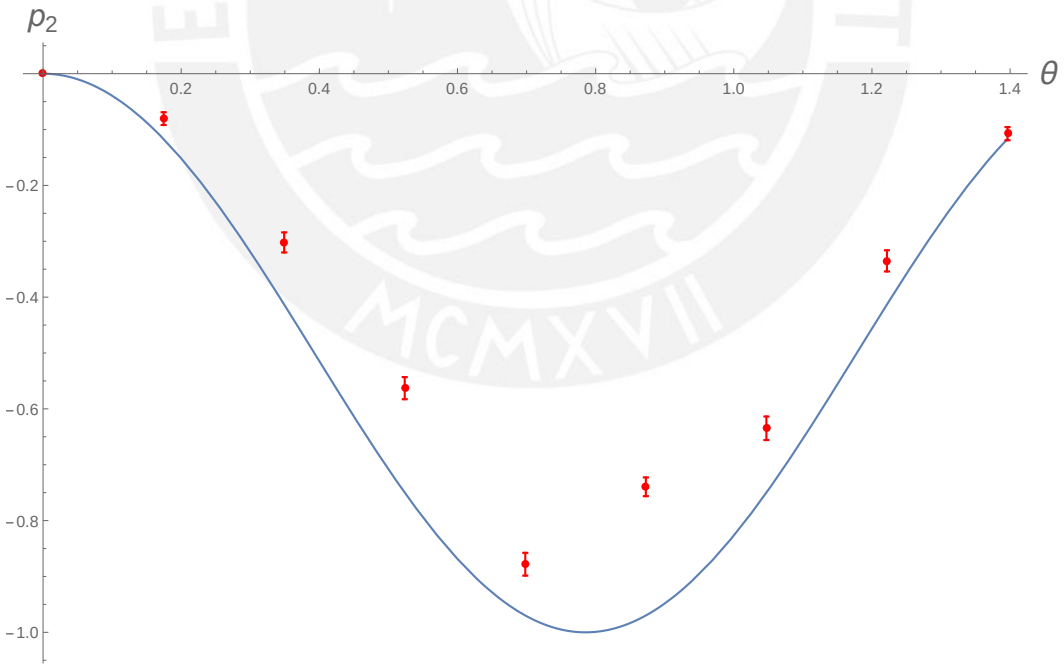

Figure 4.2: Theoretical (blue curve) and experimental (red dots) polarization Stokes parameter p_2.

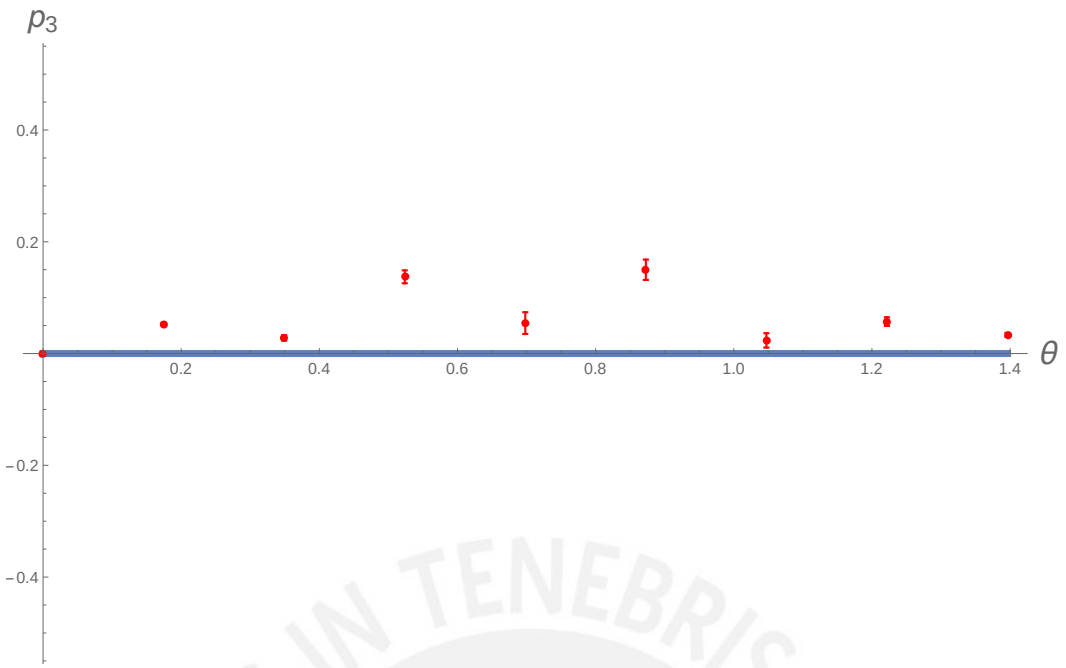

Figure 4.3: Theoretical (blue curve) and experimental (red dots) polarization Stokes parameter p_3.

4.2 Path Stokes Parameters

Since the phase ϕ_1 appears in two of the path Stokes parameters, it is evident that path tomography must be done outside the interferometer. Given our choice of transformations T_1 and T_2, the path Stokes parameters take the form

$$q_1 = \cos 4\theta, \tag{4.2a}$$

$$q_2 = \frac{\sqrt{2}}{2} \sin 4\theta \cos \phi_1, \tag{4.2b}$$

$$q_3 = \frac{\sqrt{2}}{2} \sin 4\theta \sin \phi_1. \tag{4.2c}$$

Before plotting the theoretical curves, the phase ϕ_1 had to be determined. By looking at the experimental data, we can infer which quadrant the phase belongs to. In our case, since the experimental values of $q_2 \propto \sin 4\theta \cos \phi_1$ ($q_3 \propto \sin 4\theta \sin \phi_1$) were negative (positive) for $0 \leq \theta \leq \pi/4$, we concluded that the phase was in the second quadrant. Afterwards, we calculated the ratio $q_3/q_2 = \tan \phi_1$ for each state, found its inverse tangent, reduced the angles to the second quadrant, and averaged them. This way, we found the phase to be $\phi_1 = 1.95 \pm 0.18$ rad, or $111.78° \pm 10.47°$.

Figures 4.4–4.6 show the theoretical and experimental path Stokes parameters q_1,

q_2, and q_3. The three parameters fit their curves better than the p_i fit theirs.

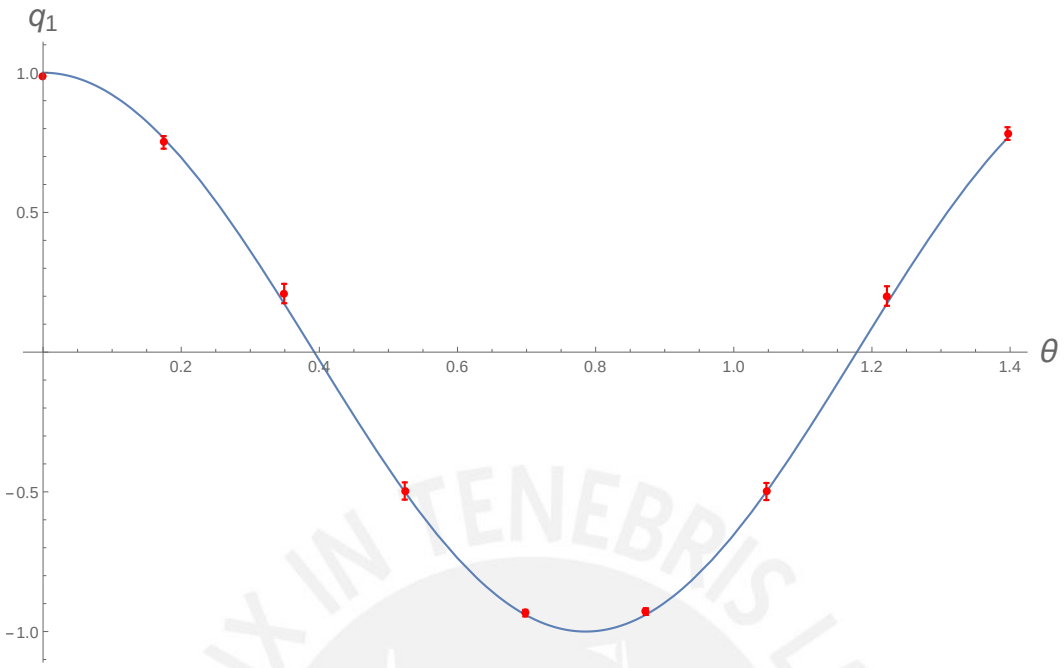

Figure 4.4: Theoretical (blue curve) and experimental (red dots) path Stokes parameter q_1.

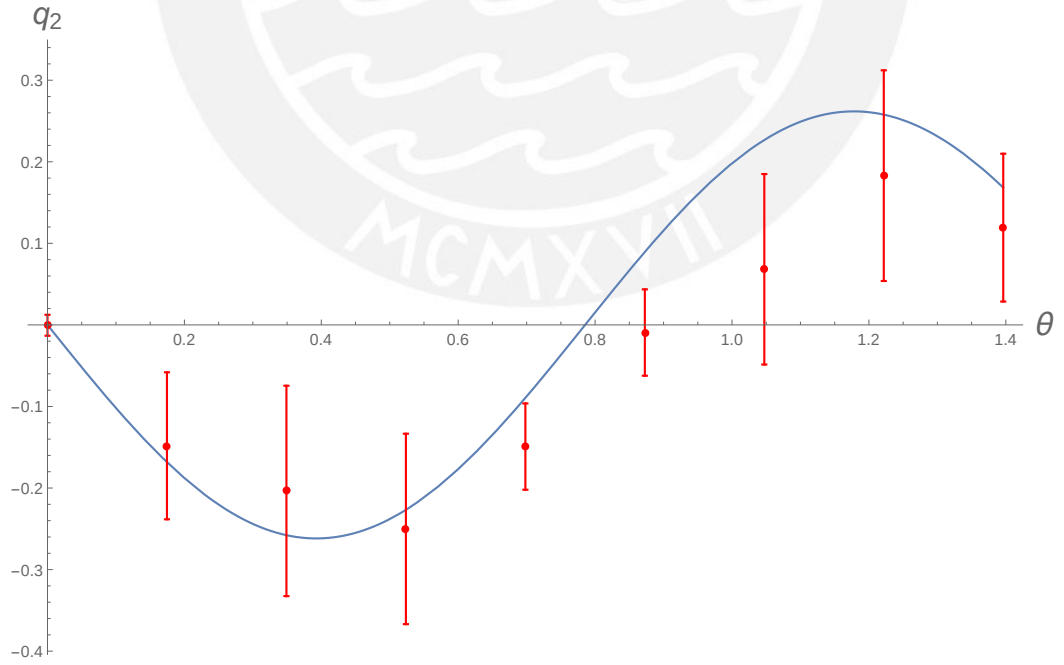

Figure 4.5: Theoretical (blue curve) and experimental (red dots) path Stokes parameter q_2.

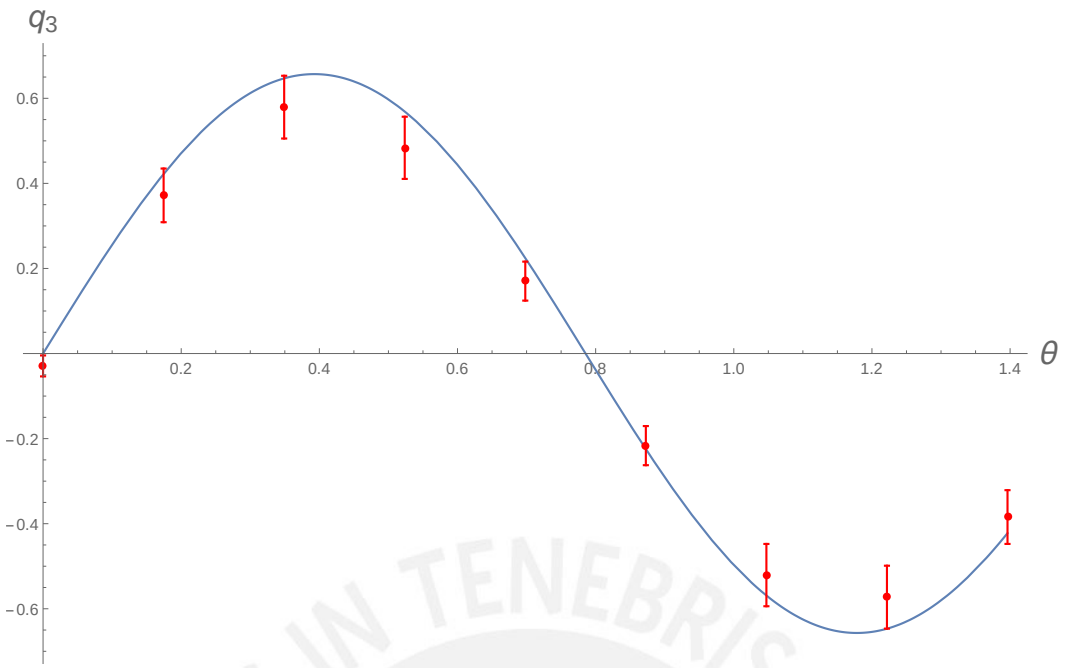

Figure 4.6: Theoretical (blue curve) and experimental (red dots) path Stokes parameter q_3.

4.3 Correlation Parameters

The correlation parameters corresponding to our array are given by

$$r_{11} = \frac{1}{2}(1 + \cos 4\theta), \tag{4.3a}$$

$$r_{12} = \frac{\sqrt{2}}{2} \sin 4\theta \cos \phi_1, \tag{4.3b}$$

$$r_{13} = \frac{\sqrt{2}}{2} \sin 4\theta \sin \phi_1, \tag{4.3c}$$

$$r_{21} = \sin^2 2\theta, \tag{4.3d}$$

$$r_{22} = -\frac{\sqrt{2}}{2} \sin 4\theta \cos \phi_1, \tag{4.3e}$$

$$r_{23} = -\frac{\sqrt{2}}{2} \sin 4\theta \sin \phi_1, \tag{4.3f}$$

$$r_{31} = 0, \tag{4.3g}$$

$$r_{32} = -\frac{\sqrt{2}}{2} \sin 4\theta \sin \phi_1, \tag{4.3h}$$

$$r_{33} = \frac{\sqrt{2}}{2} \sin 4\theta \cos \phi_1. \tag{4.3i}$$

Figures 4.7–4.15 show the theoretical and experimental correlation parameters. Save for r_{21}, r_{22}, and r_{33}, all parameters fit quite nicely to their theoretical curves. With these values, we have completely characterized all 9 states.

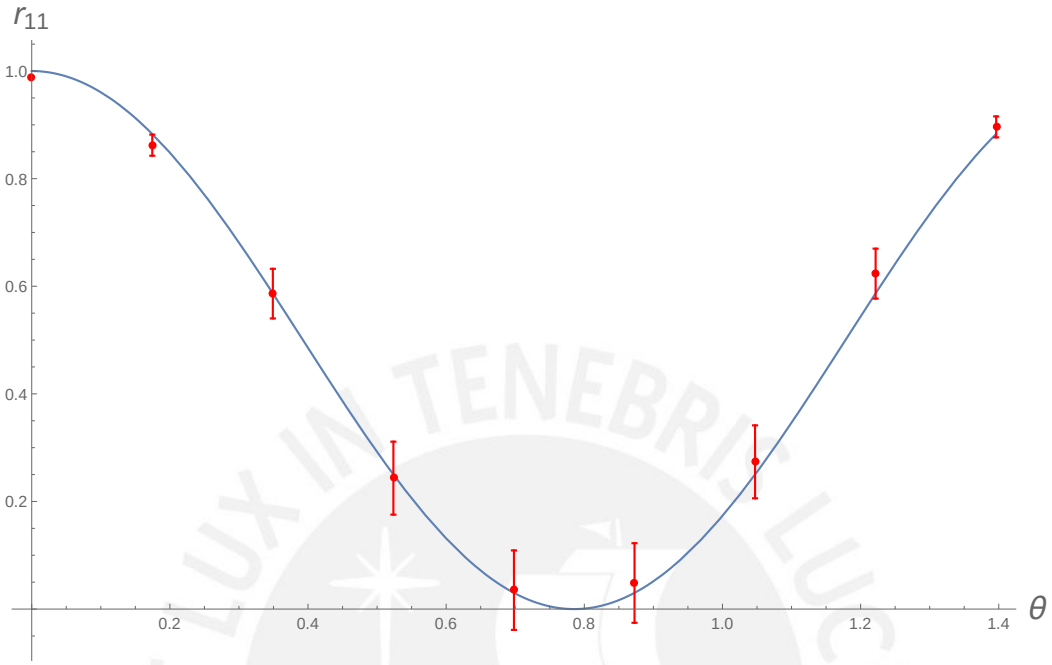

Figure 4.7: Theoretical (blue curve) and experimental (red dots) correlation parameter r_{11}.

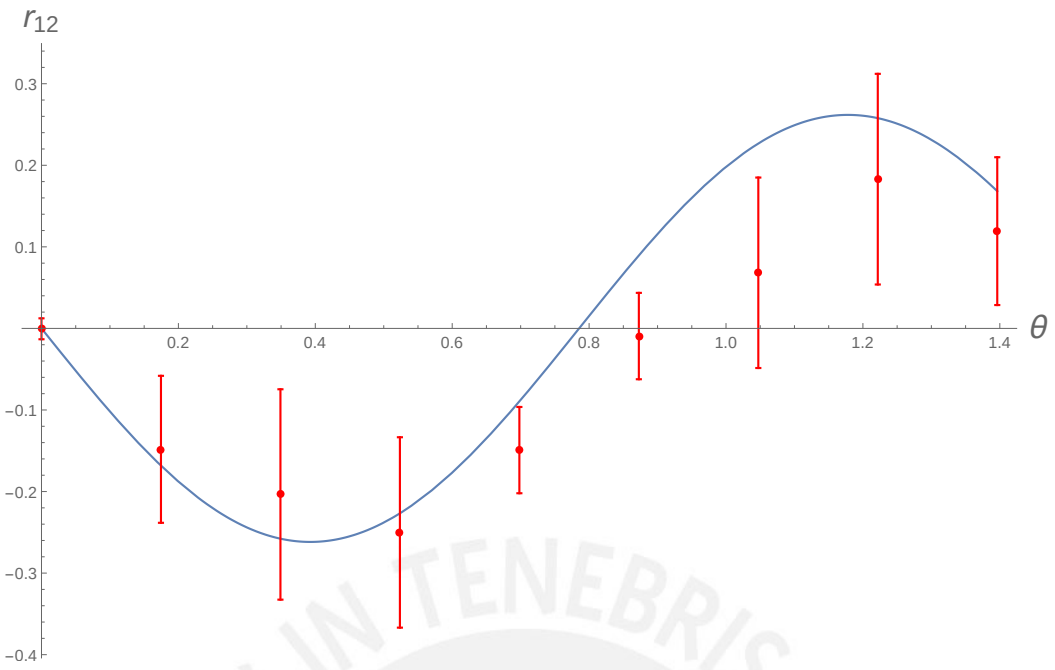

Figure 4.8: Theoretical (blue curve) and experimental (red dots) correlation parameter r_{12}.

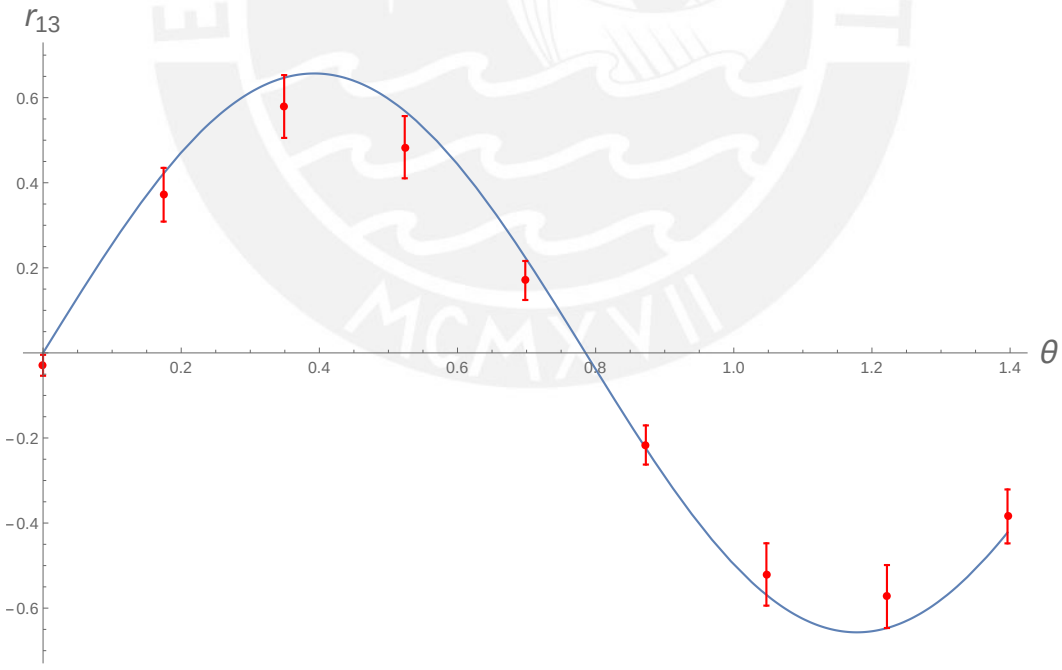

Figure 4.9: Theoretical (blue curve) and experimental (red dots) correlation parameter r_{13}.

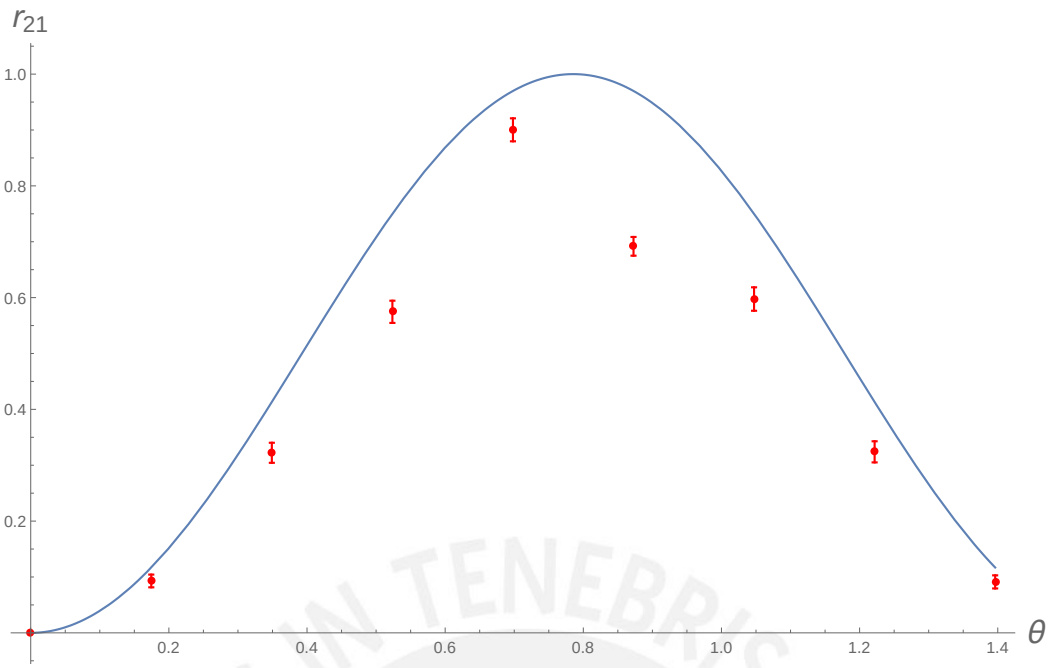

Figure 4.10: Theoretical (blue curve) and experimental (red dots) correlation parameter r_{21}.

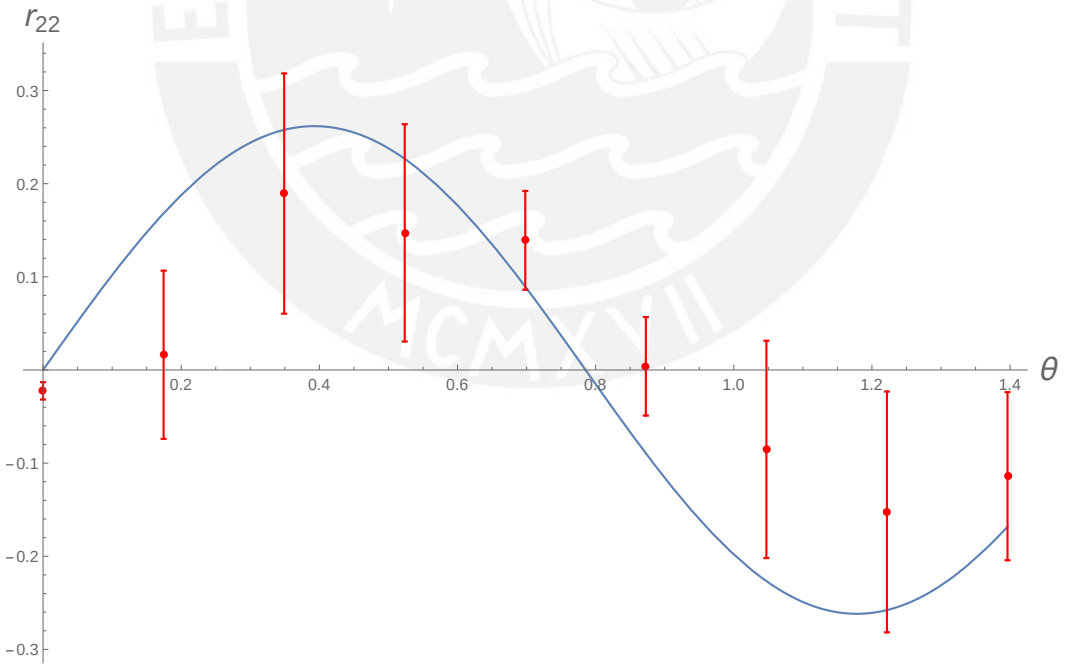

Figure 4.11: Theoretical (blue curve) and experimental (red dots) correlation parameter r_{22}.

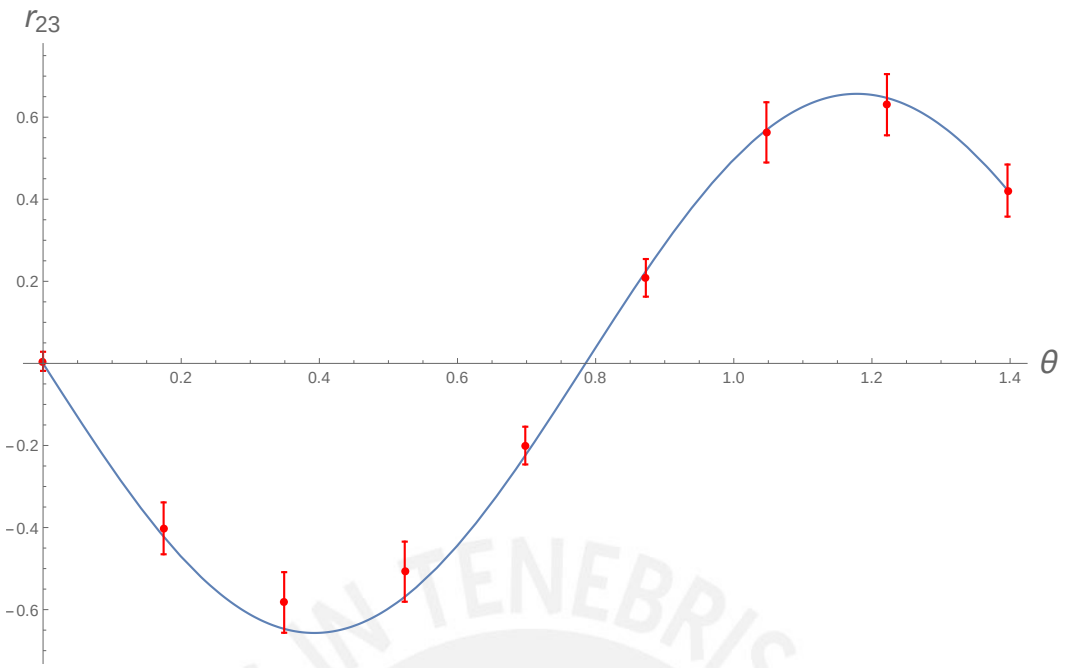

Figure 4.12: Theoretical (blue curve) and experimental (red dots) correlation parameter r_{23}.

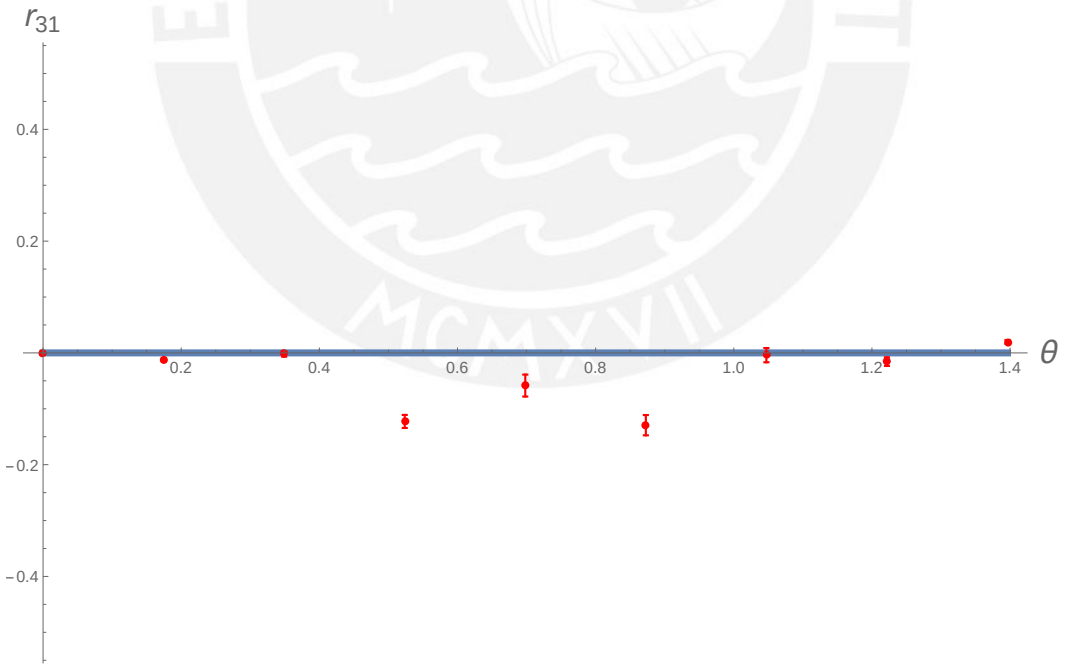

Figure 4.13: Theoretical (blue curve) and experimental (red dots) correlation parameter r_{31}.

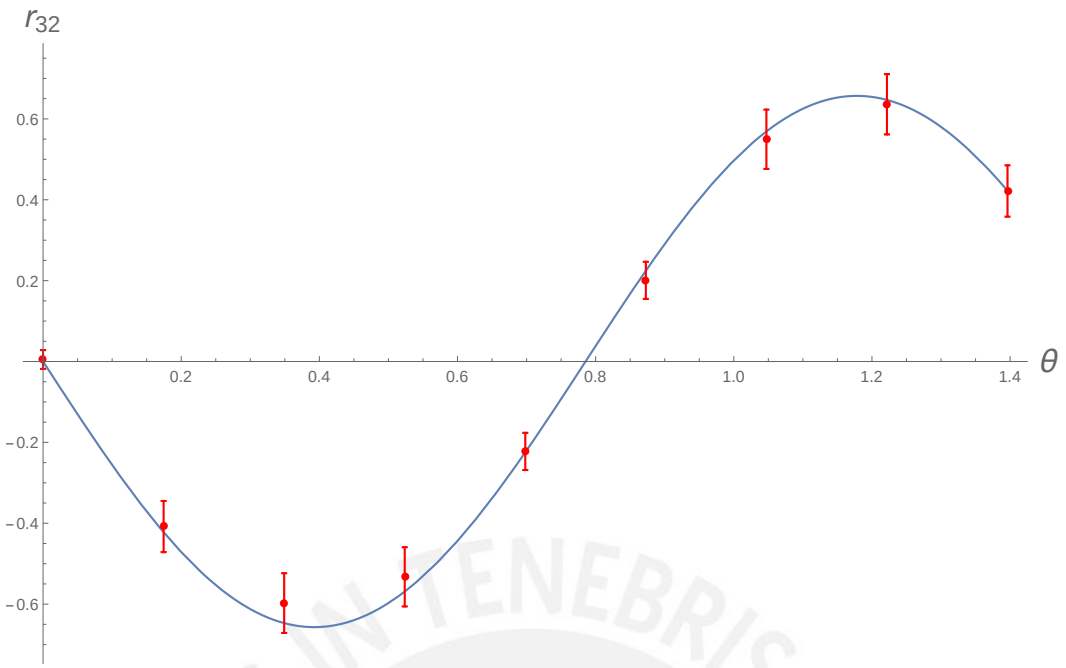

Figure 4.14: Theoretical (blue curve) and experimental (red dots) correlation parameter r_{32}.

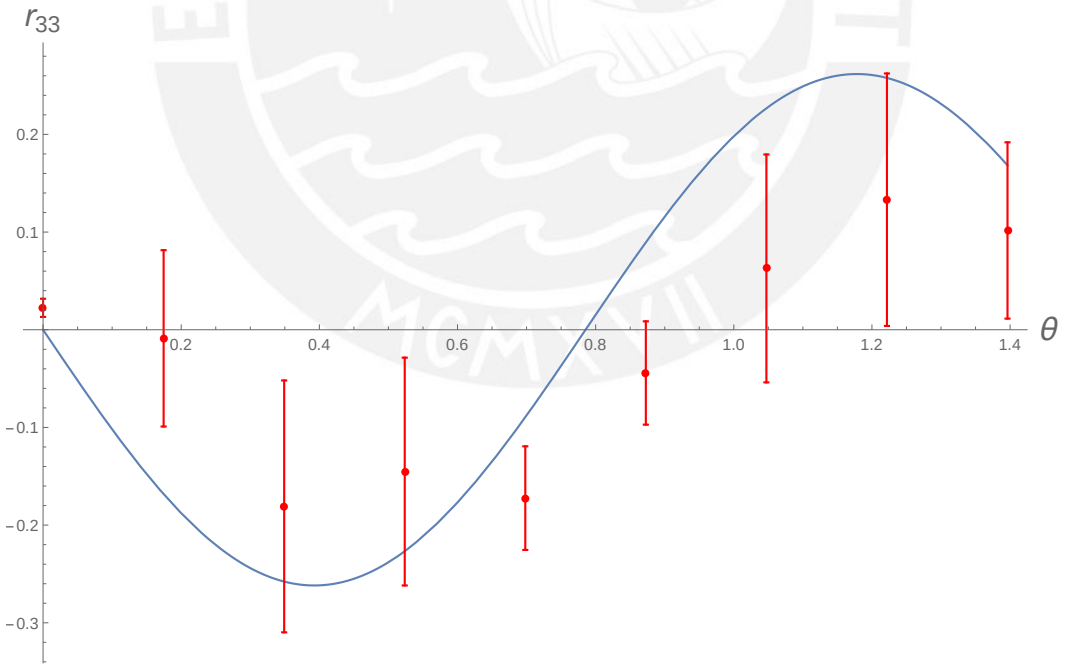

Figure 4.15: Theoretical (blue curve) and experimental (red dots) correlation parameter r_{33}.

Chapter 5

Summary and Outlook

5.1 Summary

We set out with the objective of developing a tomography algorithm that could characterize pure states of polarization-path two-qubit systems in quantum optical settings. To this end, we contrived a simple tomography gadget consisting of a Mach-Zehnder interferometer with a half-wave plate in one arm. As we are painfully aware of, this configuration can be too unstable to yield even mildly reasonable results. Luckily, we managed to devise an alternative, stable array. Said array consists of 6 half-wave plates, 1 quarter-wave plate, and two polarizing beam displacers. We prepared a set of pure two-qubit states in our interferometer and carried out a complete state tomography on them. Our results, in the form of the 6 single-qubit Stokes parameters and the 9 correlation parameters, are in good agreement with the predicted values. Therefore, our proposed tomography algorithm works as intended.

A crucial element of our algorithm is the phase ϕ_1. If the interferometer is unstable, the phase will fluctuate wildly and the measurements will yield nonsensical results. Despite our experimental phase having a relative uncertainty of 9%, we can safely say that our results represent a remarkable improvement over previous attempts. Indeed, having spent several months trying to do two-qubit tomography in Mach-Zehnder and Sagnac interferometers to no avail, we conclude, by looking at the curves in Chapter 4, that PBD interferometers are remarkably more stable than other interferometers. While far from perfect, they perform quite decently.

5.2 Outlook

There exist two main sources of error for our experimental results. First is our way of using the half-wave plates in the PBD interferometer. Since the distance between both arms is small, we had to get part of the plates cut out, so that one of the beams went through the hole and the other through the plate's fringe. However, wave plates are known to function non-ideally when the beam incides far from the center. This difficulty could be overcome by using wave plates custom-made for our array. Second are the fluctuations in the phase ϕ_1. These are significantly lower when the measurements are taken over small intervals of time, so it is advisable to measure in just a few hours. Moreover, our results could be improved by working in a more robust setting, such as a heavy optical table, and using heavy mounts for the PBDs.

The simple tomographic device of Fig. 3.2 that we have presented in this thesis can be used to test several kinds of theoretical models. Quantum evolutions such as the single qubit dissipative channel, the amplitude damping channel, the random unitary channel, and one- and two-qubit dephasing channels [12, 13] can be simulated in a PBD interferometer. Quite recently, a single-qubit dephasing channel was carried out in the path qubit of a PBD interferometer [34]. This shows that our experimental array can be used to study properties of current interest in the open quantum systems community, such as quantum (non-)Markovianity and coherence.

Additionally, the possibility of doing quantum light interferometry experiments with a PBD interferometer is currently being explored. And, last but not least, we expect that, with a few modifications, our device can be used to generate and completely characterize mixed two-qubit states—which depend on 15 parameters instead of 6. We hope that this will be the subject of future works.

Bibliography

[1] J. N. Damask, *Polarization Optics in Telecommunications*, softcover reprint of hardcover 1st ed. 2005 (Springer, 2005).

[2] D. F. V. James, P. G. Kwiat, W. J. Munro, and A. G. White, "Measurement of qubits", Phys. Rev. A **64**, 052312 (2001).

[3] J. T. Barreiro, N. K. Langford, N. A. Peters, and P. G. Kwiat, "Generation of hyperentangled photon pairs", Phys. Rev. Lett. **95**, 260501 (2005).

[4] P. Walther, K. J. Resch, T. Rudolph, E. Schenck, H. Weinfurter, V. Vedral, M. Aspelmeyer, and A. Zeilinger, "Experimental one-way quantum computing", Nature **434**, 169 (2005).

[5] J. Altepeter, E. Jeffrey, and P. Kwiat, "Photonic state tomography", English (US), in *Advances in atomic, molecular and optical physics*, Vol. 52 (Dec. 2005), pp. 105–159.

[6] C. F. Roos, M. Riebe, H. Häffner, W. Hänsel, J. Benhelm, G. P. T. Lancaster, C. Becher, F. Schmidt-Kaler, and R. Blatt, "Control and measurement of three-qubit entangled states", Science **304**, 1478 (2004).

[7] I. L. Chuang, N. Gershenfeld, and M. Kubinec, "Experimental implementation of fast quantum searching", Phys. Rev. Lett. **80**, 3408 (1998).

[8] J. Medford, J. Beil, J. Taylor, S. Bartlett, A. Doherty, E. Rashba, D. DiVincenzo, H. Lu, A. Gossard, and C. M. Marcus, "Self-consistent measurement and state tomography of an exchange-only spin qubit", Nature Nanotechnology **8**, 654 (2013).

[9] J. Gonzales, P. Sánchez, V. Avalos, and F. D. Zela, "Experimental Bell violations with entangled and non-entangled optical fields", in Latin America Optics and Photonics Conference (2018), Tu5D.2.

[10] S. Cialdi, D. Brivio, E. Tesio, and M. G. A. Paris, "Programmable entanglement oscillations in a non-Markovian channel", Phys. Rev. A **83**, 042308 (2011).

[11] A. Smirne, D. Brivio, S. Cialdi, B. Vacchini, and M. G. A. Paris, "Experimental investigation of initial system-environment correlations via trace-distance evolution", Phys. Rev. A **84**, 032112 (2011).

[12] T. Chanda and S. Bhattacharya, "Delineating incoherent non-Markovian dynamics using quantum coherence", Annals of Physics **366**, 1 (2016).

[13] Z. He, H.-S. Zeng, Y. Li, Q. Wang, and C. Yao, "Non-Markovianity measure based on the relative entropy of coherence in an extended space", Phys. Rev. A **96**, 022106 (2017).

[14] D. F. Urrego, J. Flórez, J. Svozilík, M. Nuñez, and A. Valencia, "Controlling non-Markovian dynamics using a light-based structured environment", Phys. Rev. A **98**, 053862 (2018).

[15] Z. Huang and H. Situ, "Optimal protection of quantum coherence in noisy environment", International Journal of Theoretical Physics **56**, 503 (2017).

[16] M. Passos, P. Concha Obando, W. Balthazar, F. Paula, J. Huguenin, and M. Sarandy, "Non-Markovianity through quantum coherence in an all-optical setup", arXiv preprint:1807.05378 (2018).

[17] B. Qi, Z. Hou, L. Li, D. Dong, G. Xiang, and G. Guo, "Quantum state tomography via linear regression estimation", Scientific Reports **3**, 3496 (2013).

[18] R. Blume-Kohout, "Optimal, reliable estimation of quantum states", New Journal of Physics **12**, 043034 (2010).

[19] R. Schmied, "Quantum state tomography of a single qubit: comparison of methods", Journal of Modern Optics **63**, 1744 (2016).

[20] C. Schwemmer, L. Knips, D. Richart, H. Weinfurter, T. Moroder, M. Kleinmann, and O. Gühne, "Systematic errors in current quantum state tomography tools", Phys. Rev. Lett. **114**, 080403 (2015).

[21] C. Ferrie and R. Blume-Kohout, "Maximum likelihood quantum state tomography is inadmissible", arXiv preprint: 1808.01072 (2018).

[22] M. Christandl and R. Renner, "Reliable quantum state tomography", Phys. Rev. Lett. **109**, 120403 (2012).

[23] P. Faist and R. Renner, "Practical and reliable error bars in quantum tomography", Phys. Rev. Lett. **117**, 010404 (2016).

[24] M. Cramer, M. B. Plenio, S. T. Flammia, R. Somma, D. Gross, S. D. Bartlett, O. Landon-Cardinal, D. Poulin, and Y.-K. Liu, "Efficient quantum state tomography", Nature Communications **1**, 149 (2010).

[25] C. Carmeli, T. Heinosaari, M. Kech, J. Schultz, and A. Toigo, "Stable pure state quantum tomography from five orthonormal bases", EPL (Europhysics Letters) **115**, 30001 (2016).

[26] X. Ma, T. Jackson, H. Zhou, J. Chen, D. Lu, M. D. Mazurek, K. A. G. Fisher, X. Peng, D. Kribs, K. J. Resch, Z. Ji, B. Zeng, and R. Laflamme, "Pure-state tomography with the expectation value of Pauli operators", Phys. Rev. A **93**, 032140 (2016).

[27] X. Ma, T. Jackson, H. Zhou, J. Chen, D. Lu, M. D. Mazurek, K. A. G. Fisher, X. Peng, D. Kribs, K. J. Resch, Z. Ji, B. Zeng, and R. Laflamme, "Pure-state tomography with the expectation value of Pauli operators", Phys. Rev. A **93**, 032140 (2016).

[28] J. Li, S. Huang, Z. Luo, K. Li, D. Lu, and B. Zeng, "Optimal design of measurement settings for quantum-state-tomography experiments", Phys. Rev. A **96**, 032307 (2017).

[29] O. Calderón, D. Jiménez, D. Guzmán, and A. Valencia, "Reconstrucción experimental para los grados de libertad de polarización y camino: Un paso hacia la codificación de dos qubits en un solo fotón", Momento, 92 (2014).

[30] S. Walborn, C. Monken, S. Pádua, and P. S. Ribeiro, "Spatial correlations in parametric down-conversion", Physics Reports **495**, 87 (2010).

[31] J. Schneeloch and J. C. Howell, "Introduction to the transverse spatial correlations in spontaneous parametric down-conversion through the biphoton birth zone", Journal of Optics **18**, 053501 (2016).

[32] J. J. Gil, "Polarimetric characterization of light and media - Physical quantities involved in polarimetric phenomena", Eur. Phys. J. Appl. Phys. **40**, 1 (2007).

[33] P. Štelmachovič and V. Bužek, "Dynamics of open quantum systems initially entangled with environment: Beyond the Kraus representation", Phys. Rev. A **64**, 062106 (2001).

[34] M. Uria Valencia, "Implementación y medición de un sistema cuántico abierto con la dinámica "Dephasing Channel" en la base de caminos", Master's thesis. (Pontificia Universidad Católica del Perú, 2019).